Numerical and Laboratory Investigations for Maximization of Production from Tight/Shale Oil Reservoirs: From Fundamental Studies to Technology Development and Evaluation

YEAR-END PROGRESS REPORT

October 5, 2015

Task 1: Project management and planning

This task aims to develop a plan for project management, and identify the researchers responsible for the various components of the study.

Progress in Task 1: Work on Task 1 is completed. G. Moridis is the Principal Investigator (PI), assisted by Matt Reagan (co-PI). T. Kneafsey is responsible for core-scale laboratory experiments, J. Ajo-Franklin is in charge of the nano-scale experiments and visualization, and G. Waychunas is in charge of the Molecular Fluid Dynamics Studies. G. Moridis and M. Reagan are responsible for the laboratory and field-scale simulations of shale oil production/recovery.

Task 2: Definition of metrics and methodology for screening production strategies

This task aims to define the feasibility parameters, the specific objectives and metrics of the screening study, and the corresponding methodology for the evaluation of the various strategies to be investigated. This task includes discussions among the members of the LBNL group, interactions with academia and discussions with industry specialists from companies with significant shale oil properties that are actively involved in low-viscosity fluid production from oil shale reservoirs.

Progress in Task 2: Work on Task 2 is completed. Several internal discussions of the LBNL team have led to the identification (and quantification, where appropriate) of the parameters, objectives and metrics of the study, as well as the methodology.

The first step involved the determination of the reference (base) cases, and the LBNL team decided that these have to be two: the first is the case of production from unfractured or naturally fractured reservoirs, and the second is that of production from a hydraulically (or pneumatically) fractured reservoir. The second reference case is expected to represent a significant improvement of production over that in the first reference case.

The next issue the LBNL team considered was the definition of the concept of recovery under conditions of ultra-low permeability. Activities in this task involved discussions with researchers in industry and academia. After several iterations, the LBNL agreed on a definition of "success" of recovery of shale oil that involves an increase in production (rate or cumulative) of at least 50% higher than that realized in the 2nd reference case (i.e., the one involving hydraulic or pneumatic fracturing) over a period that corresponds to the economically productive life of a shale oil well. On current evidence, this period is expected to be in the 3 to 5 year range.

Additionally, the LBNL team reached a conclusion that it is not possible to use a single metric/approach to quantify recovery. Thus, recovery in this study will no longer be represented by a single number or a range of numbers, but will instead be represented by a time-variable function of the following two quantities:

(a) As a fraction of the original oil-in-place of the volume of the reservoir subdomain defined by the well spacing (assuming standard horizontal wells)
(b) As a fraction of the original oil-in-place of the volume of the Stimulated Reservoir Volume (SRV - usually smaller than that defined by the well spacing)

Note that there other issues affecting these metrics of recovery (e.g., difficulties in describing drainage areas in heterogeneous systems), stage and cluster spacing, etc.), but it is expected that the complexities of these issues are attenuated over the chosen period of evaluation, i.e., 3-5 years.

Task 3: Evaluation of enhanced liquids recovery using displacement processes
In this task we evaluate by means of numerical simulation (involving the TOUGH+ family of codes developed at LBNL, which is already available to the project (Moridis and Blasingame, 2014)) "standard" recovery strategies involving displacement processes, accounting for all known system interactions. These include (a) traditional continuous gas flooding using parallel horizontal wells and using the currently abundant shale gas, (b) water-alternating-gas (WAG) flooding, and (c) huff-and-puff injection/production strategies using lean gas/rich gas in a traditional (single) horizontal well with multiple fractures.

Progress in Task 3: Work on Task 3 is ahead of schedule. Using properties and conditions that are typical of the Eagle Ford, Niobrara and Bakken formation (**Table 1**), we completed the investigation of displacement processes using N_2 and CH_4 as the displacement gases using parallel horizontal wells (see **Figures 1** and **2**). The studies cover the spectrum of permeability between 1 nD and 1 μD, and consider a variety of fracture types (**Figure 3**).

Figure 4 provides the results for the two base (reference) cases. The results in **Figure 5** show very little (if any difference) in recovery between the two gases despite the affinity of CH_4 for oil and the beneficial (for recovery) effects of density and viscosity reduction after CH_4 dissolution into the oil (which were expected to enhance production). This is attributed to difficulty in the diffusion of CH_4 through the displaced “bank” of oil to reach virgin shale oil. Studies on the effect of displacement by CO_2 injection are currently in progress.

An important issue on which we have been investing significant effort is the discrepancy between simulation predictions and the larger recovery of oil observed during laboratory experiments (see the description and analysis in **Appendix B**). We are in the process of identifying the reasons for the significant differences, and the initial indication is that the main cause is the estimate of permeability used in the computations.

Since May 2015, a significant effort was invested in the evaluation of the production potential of "gassy oil", i.e., oil with significant amounts of dissolved gas (mainly CH_4) at the discovery pressure. This gas is exsolved (i.e., it evolves from solution) when the pressure in the reservoir drops below the bubble point. We used properties that are consistent of the gas-oil ratio in the Bakken (1000 SCF/bbl, and a bubble point of 185 bars), and we estimated gas production for (a) the range of matrix permeabilities considered in this study and (b) for an unfractured and a fractured (Type 1) reservoir.

The results in **Figure 6** show the superior recovery of "gassy" oil vs. that of "dead" oil. Although total recovery is the same because the amount of oil is fixed in the simulation stencil we consider, recover of gassy oil is much faster for all matrix permeabilities. Additionally, early recovery is enhanced by (a) the presence of fractures and (b) an increasing matrix permeability.

In this task, a new semi-analytical solution to the problem of 3D flow through hydraulically fractured media was developed. The new solution method is called the Transformational Decomposition Method (TDM), involves successive levels of transforms that eliminate time (Laplace transforms) and space (Finite Fourier transforms) from the original partial equations of flow through geologic media, are analytical in the multi-transformed space and semi-analytical in time and space, are applicable to heterogeneous systems (**Figure 7**) and are particularly well-suited to the study of production of liquids and gases from shales. TDM can be used to analyze well tests and to determine the flow properties of producing reservoirs. Verification and validation examples are shown in **Figures 8** and **9**. **Figures 10** and **11** show respectively the pressure distribution and the curving stream lines corresponding to the 3D heterogeneous problem used for verification in **Figure 8**. More details on the TDM solution are provided in **Appendix A**.

Task 4: Evaluation of enhanced liquids recovery by means of viscosity reduction
In this task we evaluate by means of numerical simulation (using the TOUGH+ family of codes developed at LBNL) the enhanced reservoir liquids recovery strategies that are based on viscosity reduction, accounting for all known system interactions. Such strategies will include (a) flooding using appropriate gases (e.g., CO_2, N_2, CH_4) and appropriate well configurations (mainly horizontal), with the viscosity reduction resulting from the gas dissolution into the liquids, and (b) thermal processes, in which the viscosity reduction will be achieved by heating, possibly to the point of liquid vaporization and transport through the matrix to the production wells as a gas.

Progress in Task 4: Work on Task 4 is ahead of schedule. The effect of viscosity reduction here is fully represented in the studies conducted in Task 3. Additionally, we have begun investigating the effects of thermal stimulation, effected by the flow of hot fluids through horizontal wells parallel to the actual production wells. Preliminary results in **Figure 12** indicate enhancement of production, but this occurs after a significant lead time. Early heating is more effective in increasing production that heating that begins at the time of the initiation of production. In any case, the increase in production has to be further evaluated against the significant energy requirements to raise the temperature of

the low-porosity, high-heat-capacity, low-thermal-conductivity shale system, considering that the dominant heat transport mechanism in shales is the slow diffusion. More studies on the subject are in progress.

Task 5: Multi-scale laboratory studies of system interactions

The effort in this task focuses on the most promising approaches and methods identified in Tasks 2 and 3. Thus, oil-bearing samples of tight/shale formations (to be provided by Anadarko Petroleum, an industrial partner in this project) will be studied at various scales and under conditions corresponding to promising production methods. "Fresh" (i.e., recently recovered) representative media samples from at least two different reservoirs will be used.

Progress in Task 5: Work on Task 5 is on track. Samples received from an industrial collaborator in early February were deemed unsatisfactory because of excessive crumbling and age, which resulted in unacceptable quality. Following discussions and an agreement with colleagues at the Colorado School of Mines, the LBNL team secured 400 lbs of fresh, high-quality Niobrara oil shales from an outcrop in Colorado. Appropriately sized samples of the Niobrara shales were subjected to a battery of tests: calibrated CT scans for core-scale density and heterogeneity analysis, scanning electron microscopic and X-ray powder diffraction for morphological characterization, mineralogy, chemical composition, microstructure and texture analyses. The experimental apparatus for core-scale studies has been designed and assembled.

Following the completion of the laborartory apparatus, several sets of experiments were conducted. The first set involved oil displacement by means of supercritical CO2, and led to the redesign of the apparatus. The second set involved 14 experiments of depressurization and displacement using N2, and provided very interesting results that indicated higher recovery than that predicted by our numerical simulations. The study for the explanation of the discrepancy (and for determination of the cause) is in progress. A detailed discussion of the experiments, procedure, results and analysis is provided in **Appendix B**.

Finally, we reserved for late May and early June 2015 significant beam time at the Advanced Light Source facility of LBNL (the most powerful X-rays in the world) for the nano-scale study of pore-scale studies and oil flow analysis under a variety of recovery strategies. In addition to the characterization of the matrix rock and its fracturing attributes, the studies included micro-scale investigations and visualization of (a) fracture development during flow of carbonated water and (b) the effect of sweeping a propped fracture with liquid CO_2. Among the most exciting results was the observation of significant "wormholing" and pitting of the shale by the advancing CO2, which results in increased porosity and permeability. This is the first such observation, and we expect that it may have a significant impact on the production effort. A detailed discussion of the micro-scale studies can be found in **Appendix C**.

Task 6: Molecular simulation analysis of system interactions

In this task, we study the expected fluid interactions and behavior in the most promising production scenarios identified in Tasks 2 and 3, as further focused by the results in Task 4. Such fluid systems may include either mobilized oil (e.g., after a thermal treatment), or combinations of the native oil and displacing fluids (e.g., liquid water, steam, CO_2, CH_4, etc.) as well as kerogen and other high-viscosity hydrocarbons. Two types of molecular simulations are being used: Grand Canonical Monte Carlo (GCMC) simulations at constant temperature, chemical potential of the confined fluid, and pore volume, and classical Molecular Dynamics (MD) simulations at constant density (pressure) and temperature.

Progress in Task 6: Work on Task 6 is on track. In first approximation, we completed a realistic model of the pore structure using a simple slab and a cylindrical geometry. We will also develop a model of pore structure using the micro-CT data from a sample from the Niobrara formation (to be obtained from Task 5). These models allow us to obtain the thermodynamic phase behavior and fluid flow in a relatively straightforward manner as a function of the pore size. The intermolecular and intramolecular interactions are represented by effective force fields where the interaction energy is a function of intermolecular distance and several kinds of electrostatic interactions. Variations in electronic distribution are incorporated via charges placed at molecular sites. This method allows *P-T* phase diagrams to be computed directly from mixture isotherms obtained from GCMC simulations at various pressures, thus allowing one to estimate the conditions by which labile phase are present and in what proportion.

Two significant advances have been achieved in the course of this study. The first involves the geometry: this is the first representation and simulation of a pore geometry, which exposes both basal planes and edges to interactions with the fluid molecules. The second advance is the first description of flow in porous media, as opposed to all previous studies that involved static (non-flowing) fluids in pores. This was achieved by to methods (a) enhanced flow-direction-oriented gravitational forces, and (b) fluid flow with a laminar velocity profile. The simulations that are currently in progress use the LAMMPS program running on the NERSC supercomputers at LBNL. The "oil" in these simulations is either pure n-C8 alkane, or a C8 alkane with substituent species (side chain, and benzene ring). A more detailed description of the activities on the subject can be found in Appendix D.

Task 7: Evaluation of enhanced liquids recovery by means of increased reservoir stimulation, well design and well operation scheduling

In this task, we evaluate numerically the effects of enhanced reservoir stimulation (e.g., using 20-25 stimulated wells per section) on the recovery of liquids by assessing (a) the performance of enhanced stimulation, (b) improved/appropriate well designs, and (b) the effects of appropriate operation scheduling/sequencing.

Progress in Task 6: Work on Task 7 is well ahead of schedule. Although the bulk of this study is to be conducted in the 2nd year of this study, the evaluation of the importance of the fracture characteristics of the shale oil system (**Figure 3**) is at an advanced stage.

Figure 13 shows the (significant) effects of the occurrence of natural fractures on production. Preliminary results from this study (still in progress) tend to indicate that fractures (native or artificial/induced) have by far the largest positive impact on production.

References

Moridis, G.J., and T.A. Blasingame, Evaluation of Strategies for Enhancing Production of Low-Viscosity Liquids From Tight/Shale Reservoirs, Paper SPE 169479, 2014 SPE Latin America and Caribbean Petroleum Engineering Conference, 21-23 May, Maracaibo, Venezuela (http://dx.doi.org/10.2118/169479-MS).

Moridis, G.J., T. Blasingame and C.M.Freeman**,** Analysis of Mechanisms of Flow in Fractured Tight- Gas and Shale-Gas Reservoirs, Paper SPE 139250, 2010 SPE Latin American & Caribbean Petroleum Engineering Conference, Lima, Peru, 1–3 December 2010.

Moridis, G.J., and C.M. Freeman, The RealGas and RealGasH2O Options of the TOUGH+ Code for the Simulation Of Coupled Fluid And Heat Flow in Tight/Shale Gas Systems, Computers & Geosciences, 65, 56-71, 2014 (doi: 10.1016/j.cageo.2013.09.010).

Stalgorova, K. and L. Mattar, Analytical Model for Unconventional Multifractured Composite Systems, SPE Journal, 16(3), 246-256, 2013 (doi:10.2118/162516-PA)

Table 1 – Properties and conditions of the reference case (Type I)	
Parameter	**Value**
Initial pressure P	2.00×10^7 Pa (2900 psi)
Initial temperature T	60 ^oC
Bottomhole pressure P_w	1.00×10^7 Pa (1450 psia)
Oil composition	100% n-Octane
Initial saturations in the domain	$S_O = 0.7$, $S_A = 0.3$
Intrinsic matrix permeability $k_x=k_y=k_z$	10^{-18}, 10^{-19}, 10^{-20} m^2 (=1000, 100, 10 nD)
Matrix porosity ϕ	0.05
Fracture spacing x_f	30 m
Fracture aperture w_f	0.001 m
Fracture porosity ϕ_f	0.60
Formation height	10 m
Well elevation above reservoir base	1 m
Well length	1800 m (5900 ft)
Heating well temperature T_H	95 ^oC
Grain density ρ_R	2600 kg/m^3
Dry thermal conductivity $k_{\theta RD}$	0.5 W/m/K
Wet thermal conductivity $k_{\theta RW}$	3.1 W/m/K
Composite thermal conductivity model[16]	$k_{\theta C} = k_{\theta RD} + (S_A^{1/2}+S_H^{1/2})\,(k_{\theta RW} - k_{\theta RD})$
Capillary pressure model[14,23]	$P_{cap} = -P_0\left[\left(S^*\right)^{-1/\lambda}-1\right]^{-\lambda}$ $S^* = \frac{(S_A - S_{irA})}{(S_{mxA} - S_{irA})}$
S_{irA}	1
λ	0.45
P_0	2×10^5 Pa
Relative permeability Model[17]	$k_{rO} = (S_O^*)^n$ $k_{rG} = (S_G^*)^n$ $S_O^*=(S_O-S_{irO})/(1-S_{irA})$ $S_G^*=(S_G-S_{irG})/(1-S_{irA})$ EPM model
n	4
S_{irO}	0.20
S_{irA}	0.60

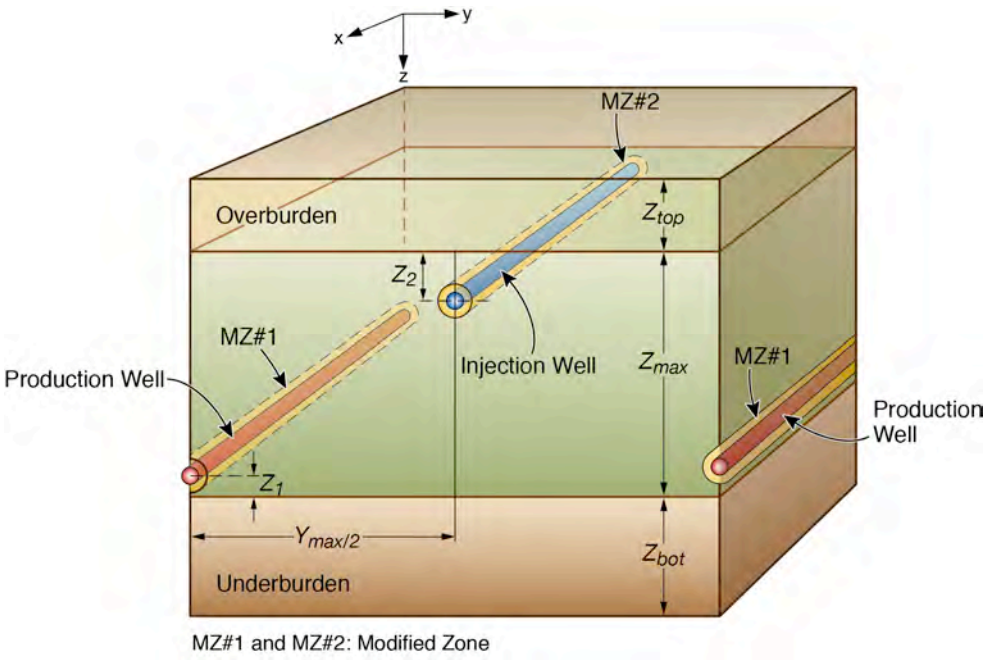

Figure 1 — Detailed stencil of the tight/shale reservoir investigated in the studies of Task 3 –View A.

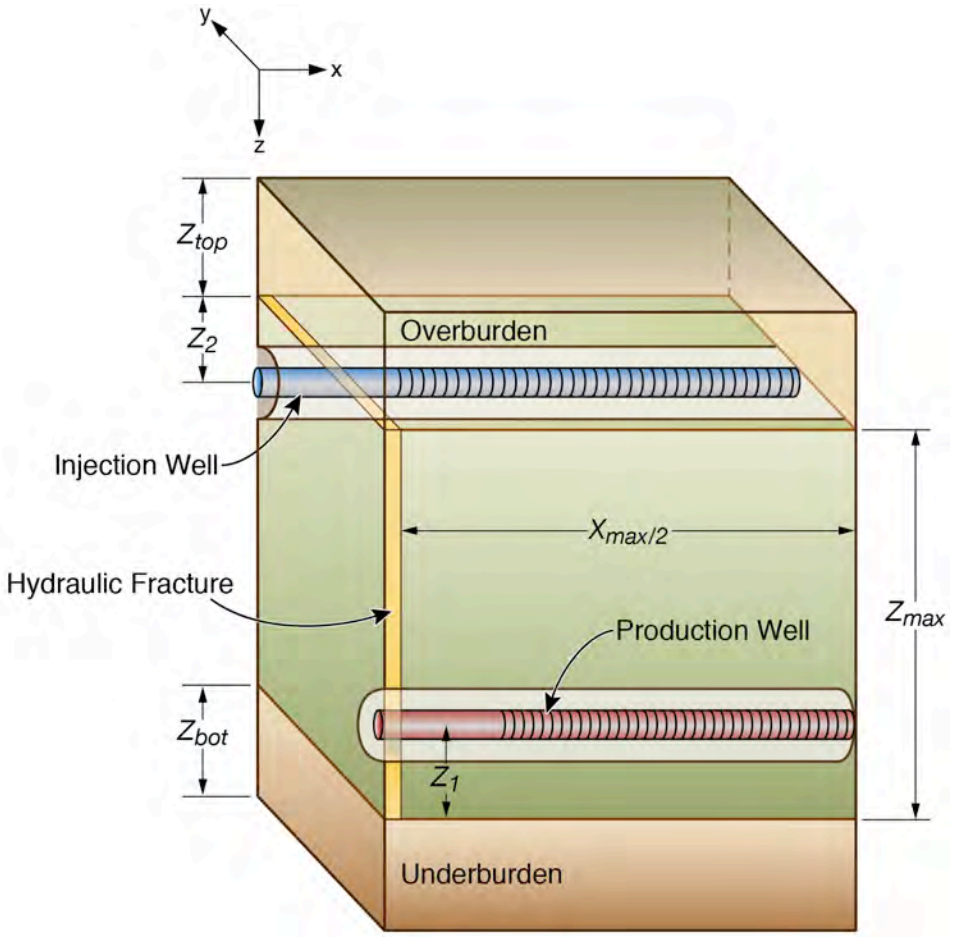

Figure 2 — Detailed stencil of the tight/shale reservoir investigated in studies of Task 3 –View B.

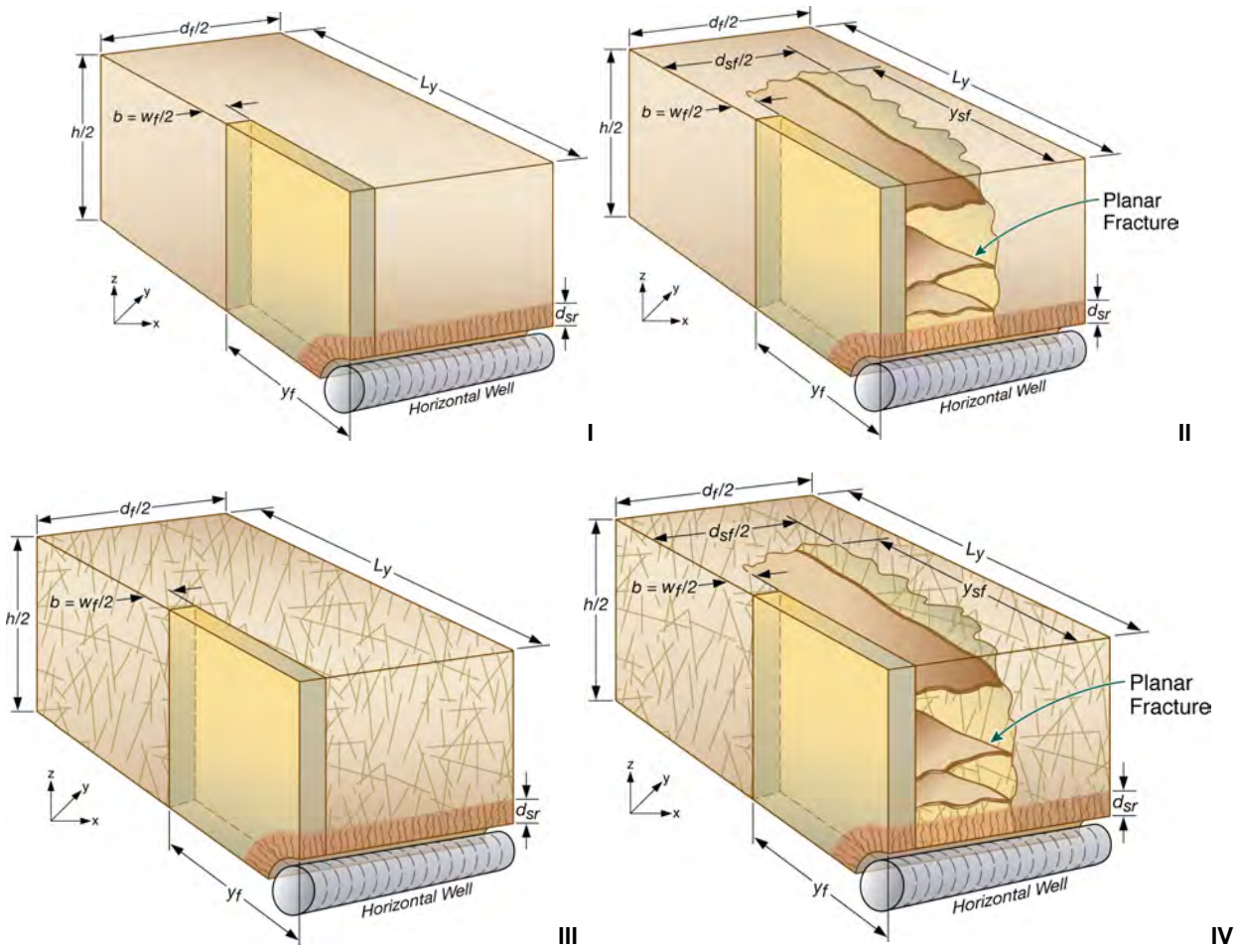

Figure 3 — Clockwise: Stencils of Types I with a hydraulic fracture), II (hydraulic fracture and stress release fractures), III (hydraulic fracture and native/natural fractures) and IV (all types of fractures) fractured systems involving a horizontal well in a tight- or shale-gas reservoir (Moridis et al., 2010).

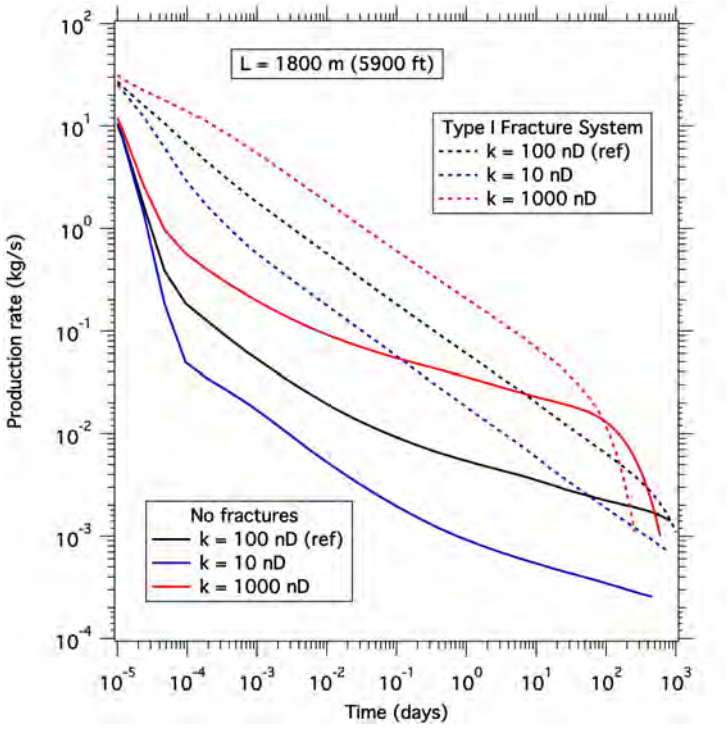

Figure 4 — Performance of the reference Cases R (unfractured) and RF (fractured), and effect of matrix permeability on the rate of oil mass production Q.

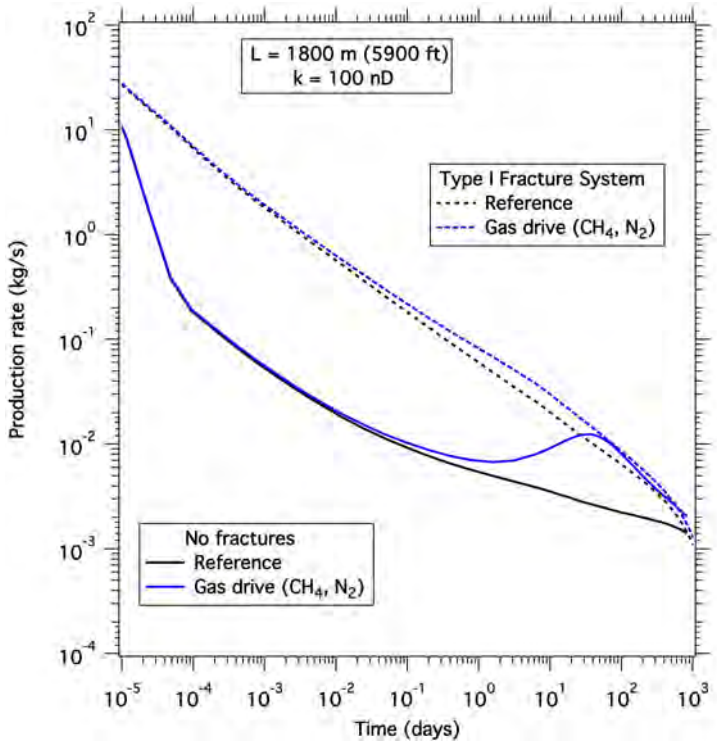

Figure 5 — Effect of a displacement process (gas drive using CH4 and N2) on Q. No discernible difference is observed between the production for CH4 and N2 drives.

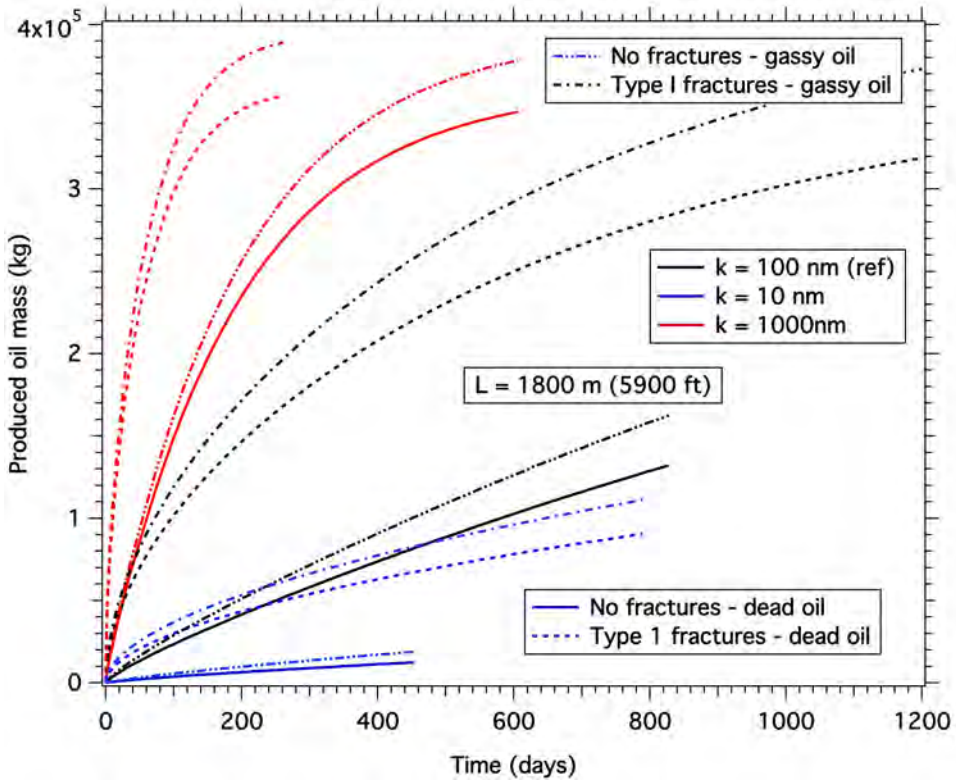

Figure 6 — Effect of dissolved gas (CH4) on oil recovery for (a) various matrix permeabilities and for (b) fractured and unfractured media. The superior recovery of "gassy" vs. "dead" oil is evident.

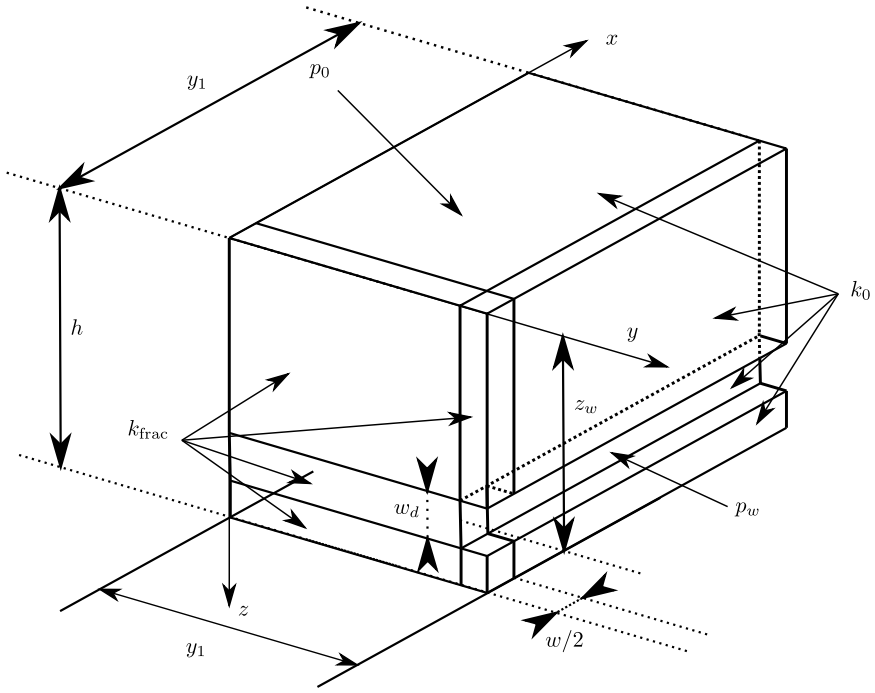

Figure 7 — Symmetric quadrant (stencil) of a heterogeneous fractured oil reservoir (heterogeneity described by different intrinsic permeabilities *k*) for comparing the TDM model against results from a TOUGH+ numerical simulation.

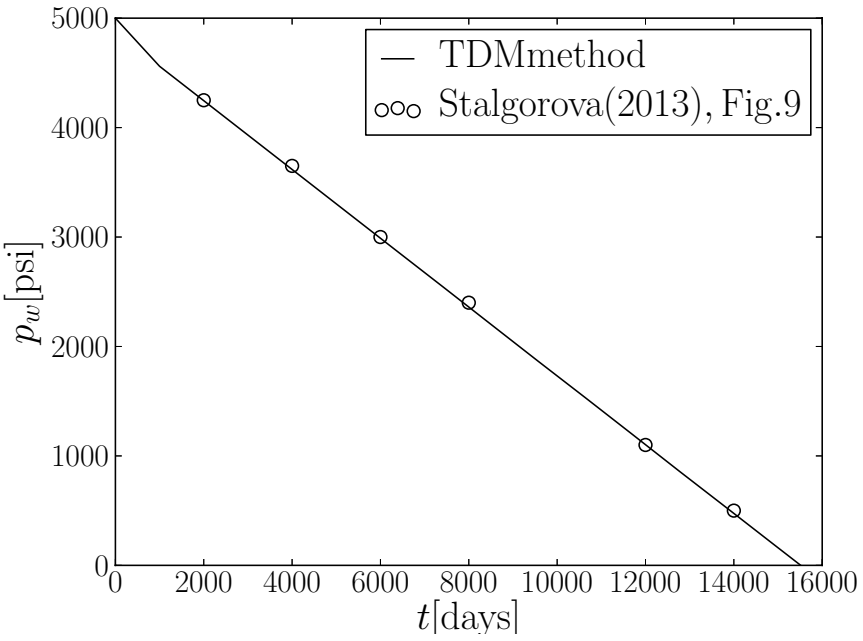

Figure 8 — Comparison of the TDM solution to the simplified semi-analytical solution of Stalgorova and Mattar (2013).

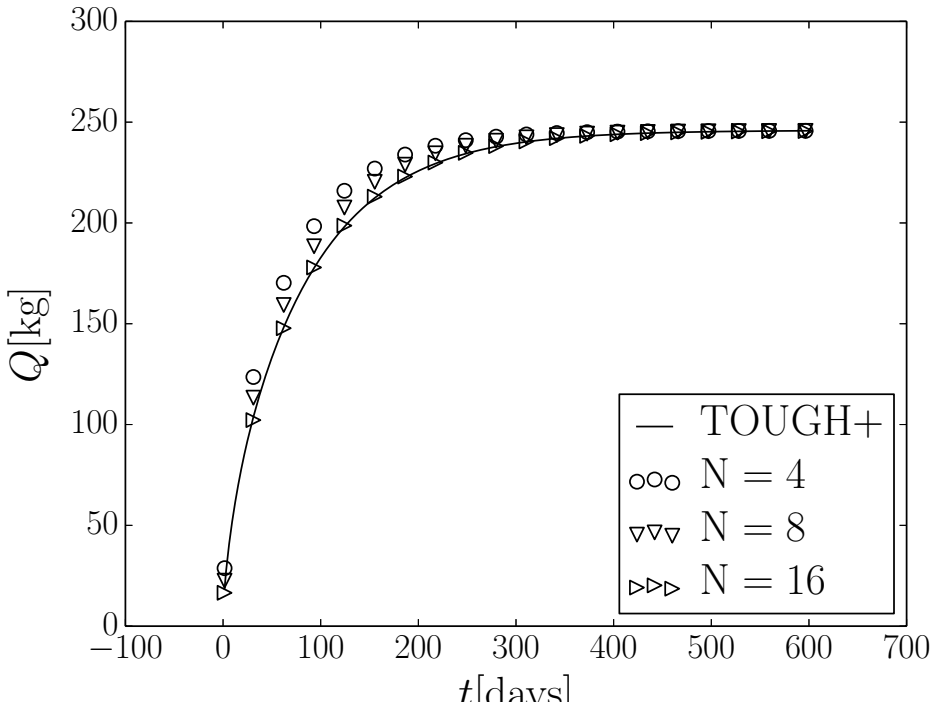

Figure 9 — Comparison of the TDM solution to the TOUGH+RealGasH2O numerical simulator (Moridis and Freeman, 2014) in a complex 3D problem with the geometry of Figure 5.

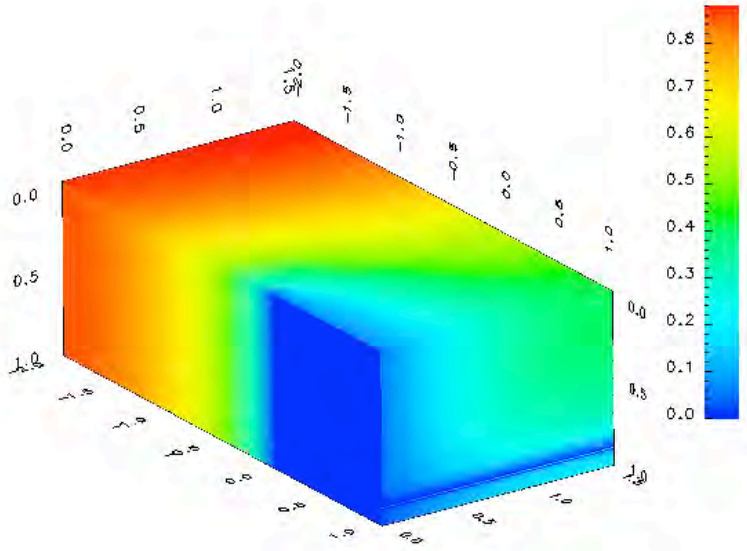

Figure 10 — 3D pressure distribution from the TDM solution in the stencil shown in Figure 5. The TDM and the TOUGH+ solutions coincide.

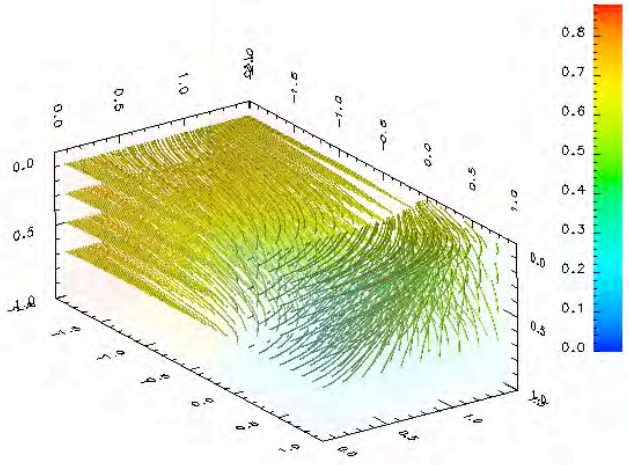

Figure 11 — 3D stream lines from the TDM solution in the stencil shown in Figure 5. The curvature of the flow lines is fully described. The TDM and the TOUGH+ solutions coincide.

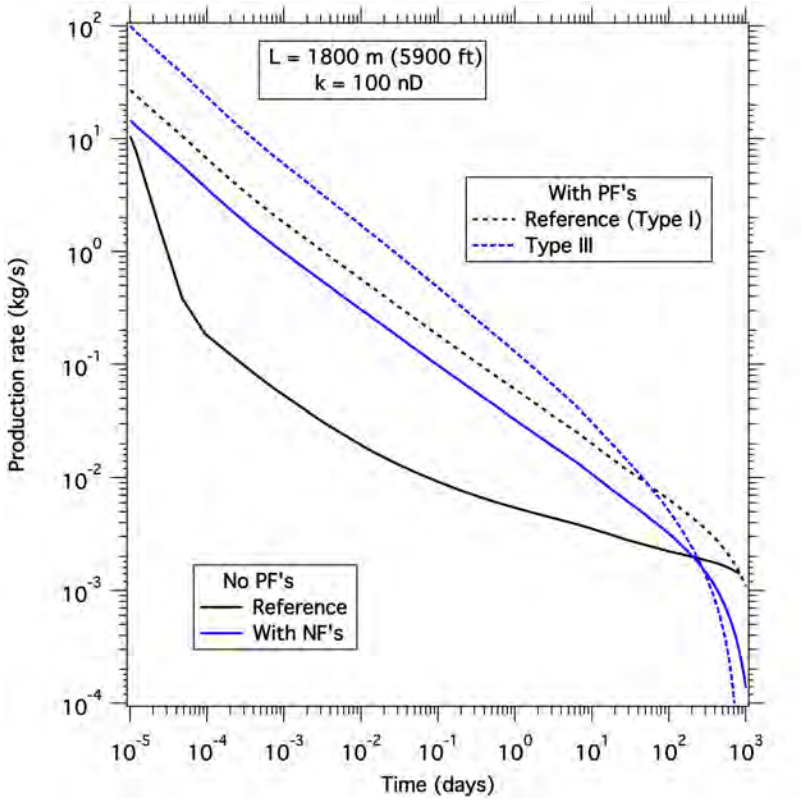

Figure 12 — Effect of the presence of native fractures (NF) or similarly-acting secondary fractures on Q. The presence of fractures has the most pronounced positive effect on production.

APPENDIX A

Progress report: Semi-analytical simulation of reservoir with heterogeneous permeability using Finite Fourier Transforms

J. K. Edmiston, G. J. Moridis

1 Summary

Low weight simulations at times may be preferable to setting up a large, high fidelity numerical simulation where generating the correct input and interpreting output are complicated by the size of the simulation, in addition to computational costs. Many of the models designed for this are only studied in the controlled production regime, which is inappropriate for unconventionals. In this note we build off the work of Stalgorova and Mattar [2] and Moridis [1] to investigate using simplified subdomain models of single phase porous flow in oil reservoirs to model production when heterogeneous permeabilities due to hydraulic fracture are present. The method employs the Finite Fourier Transform in conjuction with Laplace transformation to obtain the solution at any desired simulation time instead of forward time integration. We have verified our simulation code against both literature and high resolution numerical solutions, for both types of production regimes.

2 Recent progress

We have verified our simulation method against those given in Figs 4, 9, and 10 of Stalgorova and Mattar [2]. In that paper, a similar methodology to TD method is employed and shown to be applicable to an important range of reservoir configurations with heterogeneous permeability. In our comparison, we show that our alternative method as the benefit of being applicable to a wider range of reservoir geometries at a cost of greater computational expense (though still less than a high fidelity numerical simulation).

To employ our method for the application, we used the three-dimensional subdomain decomposition shown in Figure 1, which shows 15 subdomain regions. By exploiting the z-symmetry about the wellbore, we are able to reduce the domain size to 10 regions. Note that Stalgorova and Mattar [2] require only 5 regions. Each subdomain has a distinct permeability, either k_{frac}, k_1, or k_2, as indicated in Figure 1. The geometry and material parameters for the problems are displayed in Fig 4 and Table 1 of Stalgorova and Mattar [2]. We note a typo that the listed production rate should be 40 STB/D. Additionally, the width of the fractured region, w, is taken to be 0.25 in.

2.1 Results.

In Figures 2-4 we plot the well pressure p_w vs. time for the cases shown in Figs 6, 9, and 10 of [2], respectively. To make an easier side by side comparison we make estimates of the data shown in the relevant figures of [2] - note that these are simply visually remapped data from their figures. The figures indicates a very favorable comparison with our method. We emphasize that the reservoir

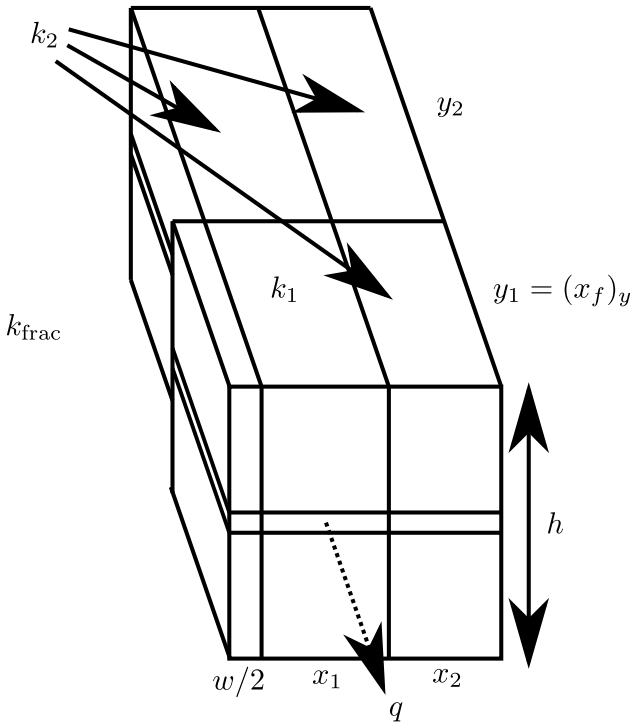

Figure 1: Oil reservoir with heterogeneous permeability, adaptation from Stalgorova and Mattar [2, Fig. 4]. For values of the displayed parameters, consult Table 1 of [2].

geometries associated with Figure 3 and Figure 4 demonstrate better matching of numerical results than their one-dimensional model.

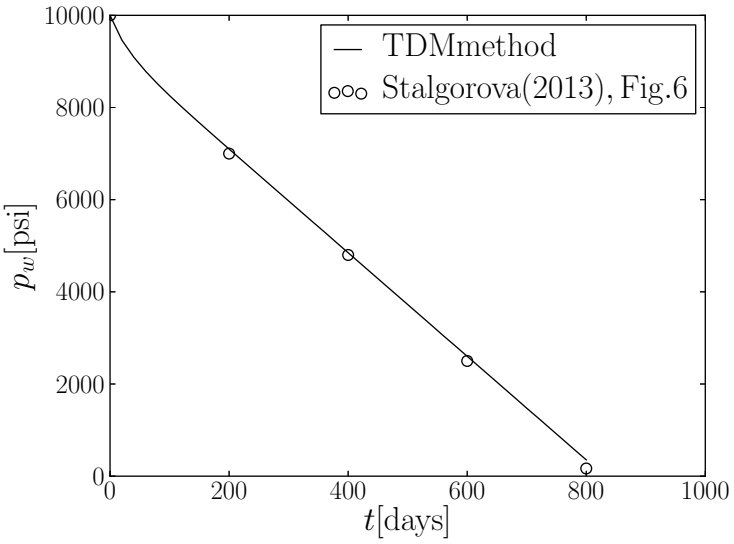

Figure 2: Well pressure p_w vs time for the simulations given in Figs 6 of Stalgorova and Mattar [2].

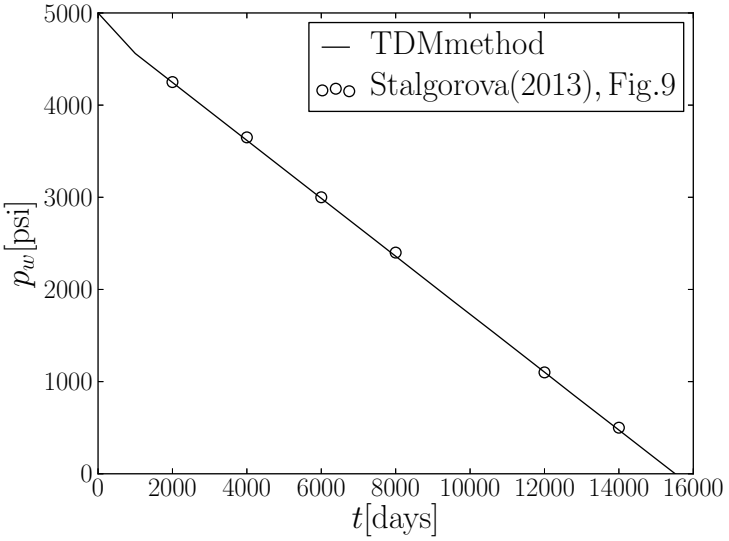

Figure 3: Well pressure p_w vs time for the simulations given in Fig 9 of Stalgorova and Mattar [2].

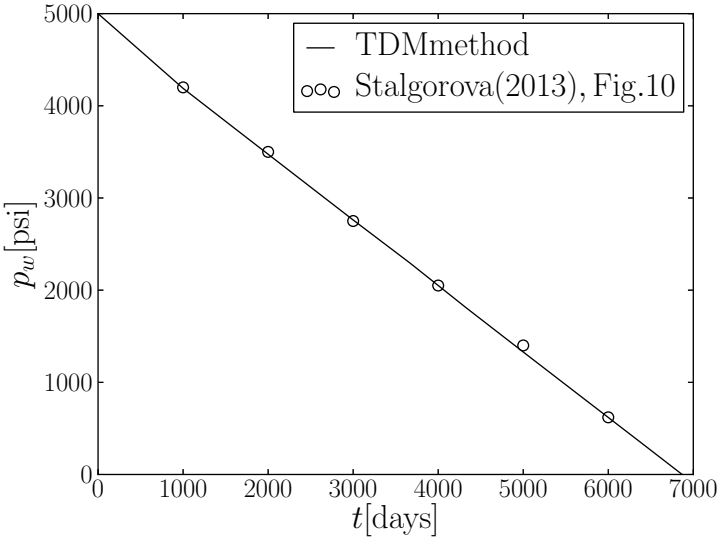

Figure 4: Well pressure p_w vs time for the simulations given in Fig 10 of Stalgorova and Mattar [2].

2.2 Pressure control boundary.

Next, we apply our method to an important boundary condition for unconventional tight oil reservoirs, where we control the well pressure instead of production rate. The problem domain we use is depicted in Figure 5. The region has been reduced by symmetry to represent one quadrant of a hydraulic fracture stage. A 10 region model required by the cut out region for the horizontal well and single hydraulic fracture. The relative scale of the dimensions of the well are exaggerated for better depiction.

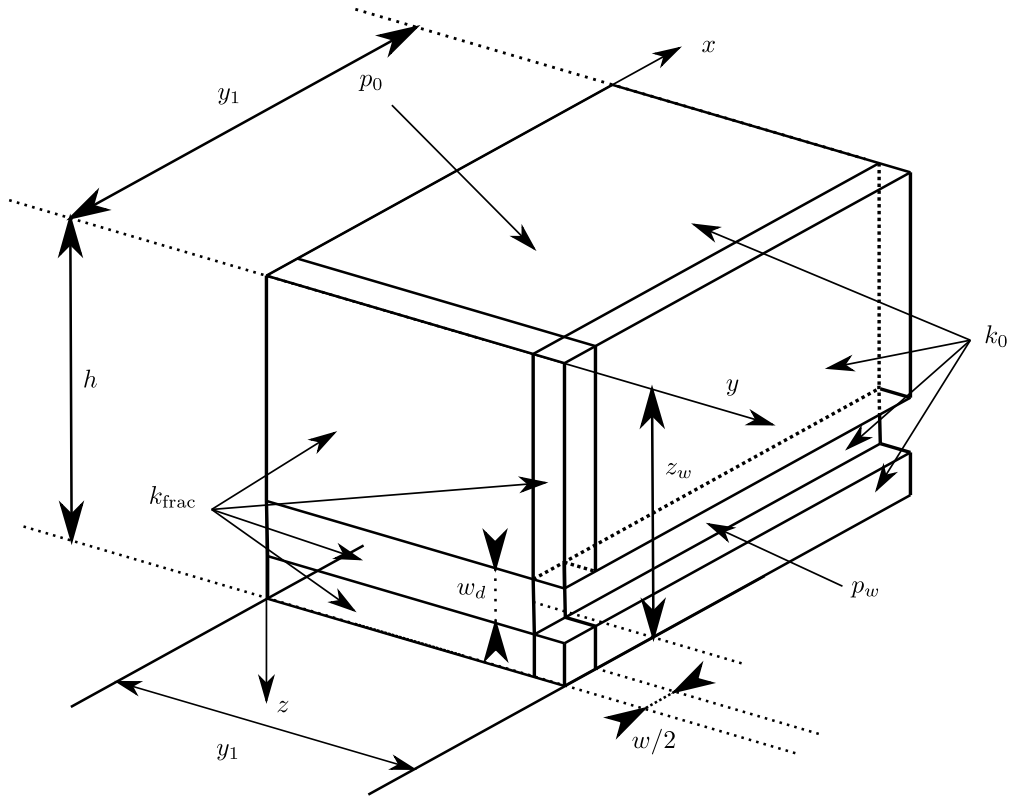

(a)

Figure 5: Symmetric quadrant of a fractured oil reservoir for comparing the TDM model against TOUGH+.

2.3 Results - TOUGH+ comparison

Figure 6 compares the production for the TD method at various levels of discretization versus TOUGH+. The legend parameter N indicates the number of terms in each of the three coordinates in the Fourier series expansion. We have approximately 10% error from the TOUGH+ solution using a coarse level of $N = 4$, which improves with increased discretization. In Figure 7 we show the reconstituted (non-dimensional) pressure distribution at $t = 4 \cdot 10^5$ seconds, along with streamlines of the pressure gradient vector field in Figure 8.

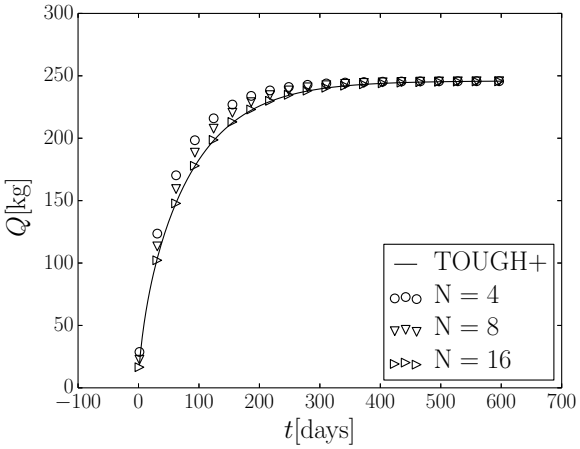

Figure 6: Figure of total produced mass at different levels of discretization.

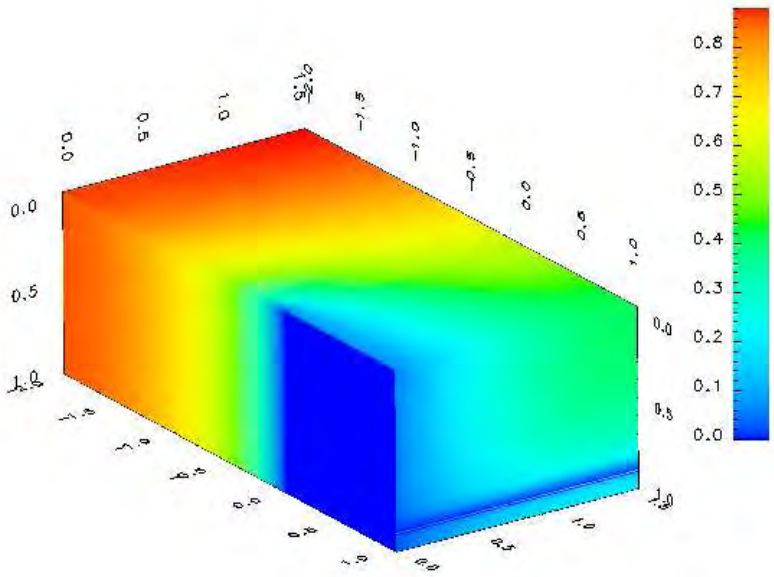

Figure 7: Non-dimensional pressure distribution at $0.4 \cdot 10^5$ seconds

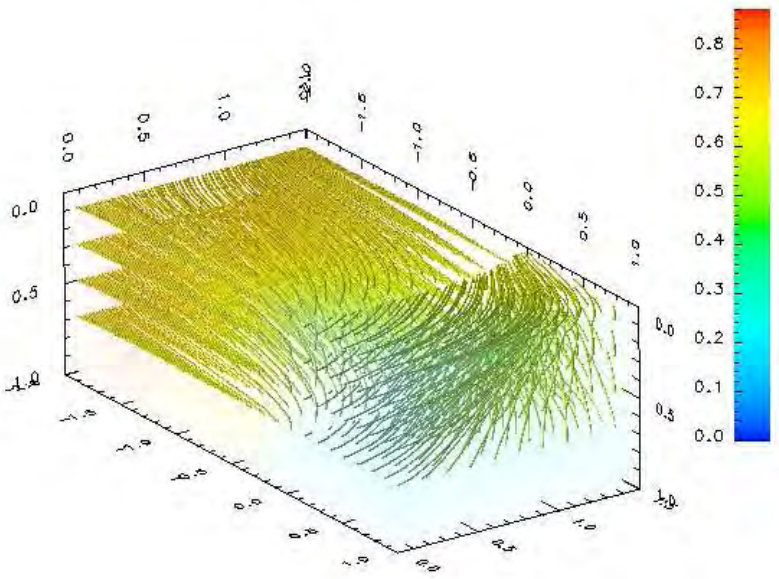

Figure 8: Streamlines distribution at $0.4 \cdot 10^5$ seconds

3 Conclusion and Future efforts

In this paper we have developed and verified an alternative simulation method which may be of use for efficient numerical modeling of reservoirs which may be approximated as several subregions with independant permeabilities. Similar models have also been proposed in the literature, however we emphasize that these models typically do not report on testing simulation performance using a controlled pressure boundary condition, which is more practically important for unconventionals. We obtained favorable comparison with both literature results and a high resolution TOUGH+ simulation. In the future we plan to iron out some numerical difficulties and make this code available to the public. For example, in the present study we used the Stehfest algorithm for inverting the transformed solutions, however we have observed temperamental numerical properties which we believe will be alleviated by using the more powerful De Hoog algorithm. The efforts to make this transformation in the code are currently under way.

References

[1] G. Moridis. The transformational decomposition (TD) method for compressible fluid flow simulations. *SPE Advanced Technology Series*, 3:163–172, 1995.

[2] Ekaterina Stalgorova and Louis Mattar. Anaytical model for unconventional multifractured composite systems. *SPE Reservoir Evaluation & Engineering*, pages 246–256, 2013.

APPENDIX B

Laboratory Investigations for Maximization of Production from Tight/Shale Oil Reservoirs: From Fundamental Studies to Technology Development and Evaluation

Core-Scale Laboratory Studies

M. Voltolini, J. Ajo-Franklin and L. Yang
Lawrence Berkeley National Laboratory

B1. Objectives

The objectives of the laboratory work performed in this task are to: 1) perform quantitative laboratory tests to investigate and quantify differences in possible light tight oil (LTO) production techniques suggested by numerical investigation, and 2) provide feedback to simulations.

B2. Production Techniques

Production techniques currently considered include depressurization (liquid phase only), depressurization with gas production and gas expansion, fluid dissolution into oil and subsequent production, water-flood, and surfactant flood.

In depressurization, fluid expands upon the lowering of pressure and "spills" into fractures (**Figure B1**). In depressurization with gas expansion, the depressurization results in the fluid expansion as before, but additionally gas present or exsolving from the oil and expanding in pores drives oil out adding to producible oil. In fluid dissolution into oil, a soluble fluid is introduced. This fluid has a low viscosity and low boiling point like scCO2 or propane. Upon mixing, the oil flows more easily and is easier to produce. Subsequent depressurization with possible gas production from the introduced fluid will drive more oil into fractures. Water flooding relies on the imbibition of water into the rock displacing oil. Surfactant flooding relies on injection of a surfactant that will reduce the interfacial tension allowing greater oil drainage.

Each of these techniques has drawbacks and uncertainties. Included in these are that depressurization and depressurization with gas drive depend on the very small fluid compressibility (less so for gas drive), the small increase in effective stress, and the low rock permeability, thus is rock block size dependent as well. Fluid dissolution depends on mixing with the oil in place. In the very stagnant pores, mixing will be limited to diffusion, unless other interfacial or chemical gradient driven processes are present. Because water flooding depends on water imbibition to drive out oil, it is doubly dependent on permeability, but also on the different types of permeability as the oil and water phases may access different pores. Liquid-phase surfactants also suffer from transport limitations. Interestingly, if a reasonable gas-phase surfactant were available, it might access the desired interfaces more easily, however a drive mechanism will also be needed.

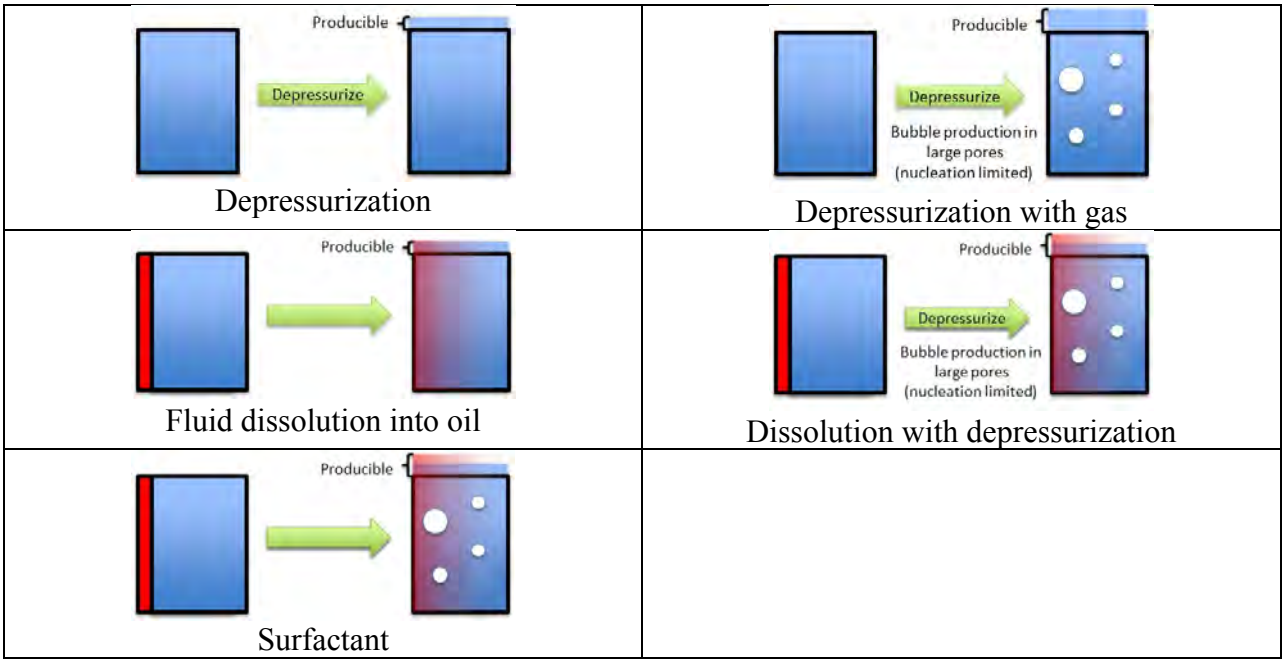

Figure B1. Process schematics.

This leads to the development of strategies that might be used. An example might be initial production from depressurization, with secondary production enhanced by re-pressurizing with gas and shutting in the well to allow dissolution into the oil and further depressurization.

Regarding laboratory tests, quantification of *processes* is important, and laboratory space and time scales must be considered. Using depressurization as an example, oil expands on depressurization and flows into lower pressure fractures. If porosity is assumed to be 5%, saturation 50%, compressibility (e.g., dodecane at 293K) 8.63×10^{-5}/MPa, then depressurizing $1 m^3$ of shale by 1MPa will eventually produce 2.15 mL of oil. This amount is quantifiable, but requires a huge relevant sample, long time, and the ability to collect a pristine, yet well characterized sample. Comparison to other processes would be daunting and the error bars high.

B2. Laboratory Tests Performed in the First Year of the Study

B2.1. Supercritical CO2 extraction of Niobrara shale

We performed a test to give us a preliminary understanding of producing oil from shale. We constructed a system to extract oil from an outcrop Niobrara shale sample. We crushed the shale to maximize the surface area to volume ratio and allow rapid mass transfer. The shale was placed in a pressure vessel and supercritical (sc) CO_2 was applied for a week to the heated vessel (**Figure B2**). Following that, the vessel was slowly drained into the cool vessel below the heated vessel. The vessel was depressurized through water. After venting, the vessel mass was slightly greater and the water developed a clean oil sheen.

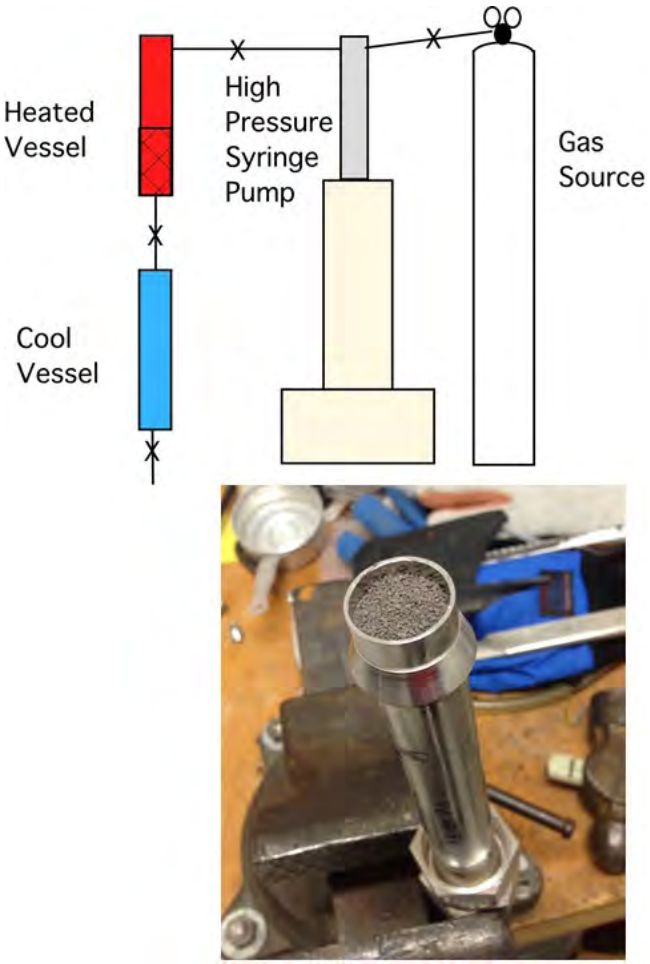

Figure B2. scCO2 extraction. Top – experiment schematic, bottom – crushed shale in pressure vessel.

Although the scCO2 extracted oil from the shale, a number of issues were identified. Included are that only a small amount of oil was produced from a very poorly characterized shale sample. To accurately quantify the oil, another extraction step would be required to remove the oil from the cool vessel, and a better way of collecting the oil compounds in the vented phase would be needed. The oil production would depend on the exact characteristics of each sample, in addition to the technique. With error bars computed, the comparisons may be difficult to make.

In response to these issues, we redesigned our tests to allow for better comparisons (**Figure B3**). To do this, we would like a large oil mass compared to the measurement error, a known oil with well understood properties, a known pore space, known mineral phase wettability, specified starting conditions, and allowing for lab-scale test durations. We selected a system that uses layers of high-porosity well-studied ceramics with water-wetting surfaces to provide an anisotropic medium that optimizes oil mass vs. measurement error, uses low vapor pressure dodecane as the oil, allows specified starting conditions, and test durations on the order of days to weeks.

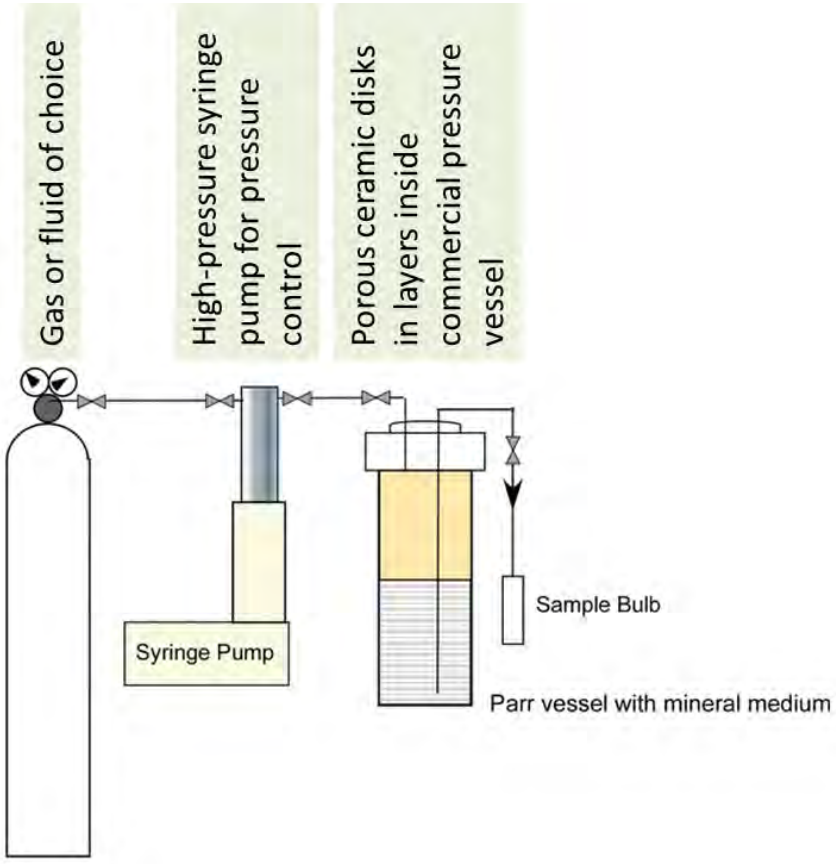

Figure B3. New System. Mineral medium (water-wetting porous ceramic disks) are preconditioned with water vapor, then vacuum/pressure-saturated with dodecane.

B2.2. Depressurization tests

To perform depressurization tests, mineral medium (water-wetting porous ceramic disks) was purchased from SoilMoisture Equipment. These discs are manufactured from alumina and are inert to most solutions. The manufacturer specifications give an effective pore size of about 2.5 microns and hydraulic conductivity of 8.6×10^{-6} cm/sec. The discs are 5.4 cm diameter, 1 cm thick with a measured average porosity of 48.1%. Prior to pressurization the discs were preconditioned with water vapor by placing them in a sealed container with water-saturated air until the discs reached constant weight, which on average was determined to be 1% water by weight (0.45 g per disc). Although these parameters do not match those of any shale, they allow for a comparison of processes on the time scales of interest.

Using the measured disc porosity, the amount of void space available for dodecane and water sorption is 11.33 cm^3. If 0.45 cm^3 of the void space is occupied with water, then 10.88 cm^3 is available for dodecane. At 1500 psi and converting to weight units this would be 8.1930 g/disc, or 65.5437 g for 8 discs (8 discs were used for each experiment). Masses of the total pore volume of dodecane at test pressures are listed in **Table B1**.

The purpose of the initial experiments has been to evaluate the reproducibility of the experimental system and sensitivity of experimental procedure. All experiments that have been completed have followed the same basic structure. This procedure has been to place 8 preconditioned discs in a standard 600 mL pressure vessel, flood with dodecane to a height which covers all the discs, and pull a vacuum on the system for 30 min to draw air out of the disks. The pressure vessels are currently kept at room temperature (this is an experimental variable) and both temperature and pressure of the vessel are logged electronically every 20 seconds. Pressure vessels are placed at an angle and dodecane is collected through a stainless steel tube which has an inlet located at the very bottom of the vessel. When sampling, pressure within the vessel drives dodecane from the vessel when a valve is opened, while desired pressure is maintained with a syringe pump. Two pressure vessels have been set up to increase the number of replicates and experimental conditions tested.

After addition of dodecane and degassing, the system is pressurized to 1500 psi with N_2 and allowed to equilibrate for a minimum of 16 hrs (overnight). Enough dodecane is added so that under pressure and with maximum absorption all the discs are covered with dodecane (no N_2/disc direct interface). The dodecane is then allowed to drain under pressure (1500 psi). Initially a large volume of dodecane is drained (on the order of 140 g) and then the system is allowed to sit and slowly drain to assure all non-sorbed dodecane is collected. Once drainage is determined to be complete, the depressurization test is performed by first reducing pressure from 1500 psi to 1000 psi and allowing the system to drain for a minimum of 16 hours. Collection of dodecane is repeated for 500 psi, 250 psi, and 0 psi (vent) until discs are returned to saturated conditions at 0 psi. The first several experiments were disassembled after the experiment to test both amount of dodecane remaining on the discs and well as the efficiency of the dodecane removal technique and it was determined that mass balance of dodecane added/dodecane recovered was greater than 98%. Following experiments were repeated without removing the discs.

Fourteen separate experiments have been performed and are summarized in **Table B2** below. In Experiment 1 insufficient dodecane was added so there was a N_2/disc interface after pressurization to 1500 psi which likely resulted in entrainment of pressurized N_2 into the discs and subsequent larger recovery of dodecane during depressurization. Included in the table are times in minutes of each pressurization/despressurization step, as well as the mass in grams of dodecane collected. All mass measurements were made at room pressure and temperature.

The predicted mass of dodecane that would be produced due to density change upon depressurization only can be calculated. If we assume 65.5437 g with a volume of 87.04 cm^3 is absorbed into the discs at 1500 psi, that same mass will have a volume of 87.3124 cm^3, a change of 0.2724 cm^3, or 0.2032 g at 0 psi. On average from the experiments the amount collected is 0.35 g, or approximately 0.47 mL, 170% of predicted. This may be due to experimental error, but the overproduction of dodecane increases at lower pressures. If the same 87.04 cm^3 is in discs at 1000 psi, then at 500 psi 0.2115 g should be produced, but on average 2.46 g, or 3.30 mL, is collected. When the pressure drops to 250 psi and 0 psi, again there is more production than density changes alone can predict. Overall, on average 8.1 g is produced whereas the predicted was ~0.8 g. Therefore in addition to density changes there are other physical processes occurring to produce oil from the discs.

One explanation for the increased production is dissolution and diffusion of nitrogen gas into the dodecane. After depressurization the system is allowed to drain for a specified period of time. During this time the exterior surfaces of the discs are exposed to nitrogen at pressure. The addition of nitrogen into already saturated discs will displace some dodecane, which could cause additional production. However the bulk of the dodecane is collected quickly after depressurization and generally only a small amount of nitrogen is added over the drainage period, so this cannot account for an order of magnitude increase in dodecane recovered. Mixing of nitrogen with dodecane will also change viscosity, surface tension and density, which could potentially increase the amount of dodecane recovered. More investigation is needed to determine the magnitude of these effects, but again these would cause changes over a period of time during diffusion, not instantly when the pressure is dropped. Lastly, and perhaps dominantly, dissolved nitrogen can expand rapidly during depressurization, displacing dodecane during expansion.

If the depressurization and nitrogen gas drive is the mechanism for increased recovery of dodecane, then longer drainage times should increase the amount of dodecane recovered due to increased time for diffusion of nitrogen into dodecane. A series of depressurizations were performed that varied the time the system was drained at 1500 psi (when the discs would be exposed to N_2 gas at 1500 psi) until depressurization at 1000 psi (Figure xx). However, so far there is only a weak correlation between either the amount of dodecane recovered at 1000 psi and the drain time at 1500 psi, or the total amount of dodecane recovered. Additional tests at a longer drain times are in process to confirm.

Diffusion rates of gas into liquids is dependent on both pressure, temperature and viscosity of the fluid. To date, a diffusion coefficient for N_2 in dodecane at 1500 psi (10 MPa) has not been found in the literature. Upreti and Mehrora (2002) report a diffusion coefficients of N_2 in bitumen at 25°C of 1.80×10^{-7} m^2/s at 4 MPa and 5.55×10^{-11} m^2/s at 8 MPa. Jamialahmadi et al. (2006) reports a diffusion coefficient for methane gas into dodecane at 10 MPa of 9.0×10^{-9} m^2/s. Methane is a bit smaller (FW 16) than Nitrogen (FW 28) but these coefficients could be used as a starting point for estimating diffusion rates.

Nitrogen density changes from 0.11628 g/cm^3 at 1500 psi to 0.0793 g/cm^3 (**Table B3**) at 1000 psi which is a more significant change in volume than dodecane over the same range. Using this to account for the excess recovery of dodecane of about 0.2 mL, 0.01586 g of N_2 would have to diffuse into the dodecane at 1500psi. To achieve the measured 2.5 g (3.4 mL) of dodecane recovered at 500 psi, 0.137 g of N2 would have to expand. Modelling of the diffusion of N2 into the discs would have to be used to estimate if these amounts are reasonable or expected during the duration of the experiment.

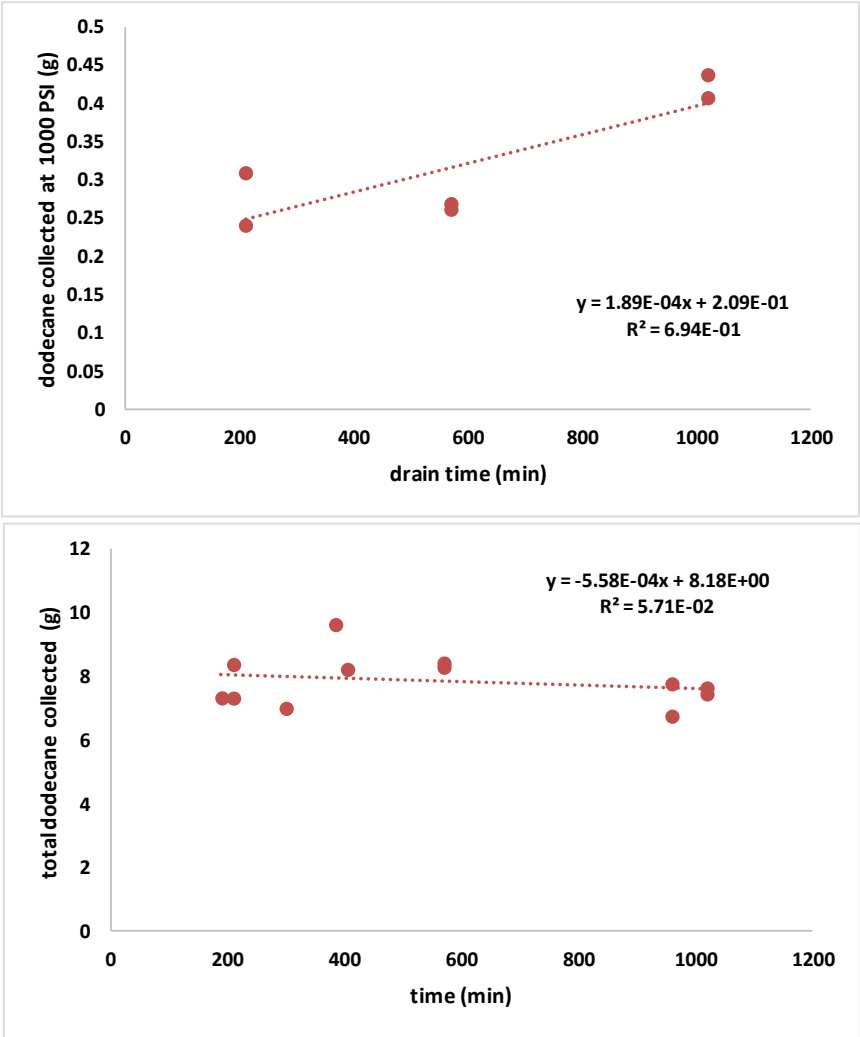

Figure B4. Top - Dodecane produced in the first depressurization versus the initial drainage (nitrogen-dodecane contact) time. Bottom – Total dodecane produced over all depressurizations versus the initial drainage time.

Table B1. Mass of 10.88 g dodecane in experiment at tested pressures.			
Pressure (psi)	Density (g/cm^3)	Mass dodecane per disc (g)	Mass dodecane per 8 discs (g)
0	0.74573	8.1135	64.9083
250	0.74693	8.1266	65.0128
500	0.74825	8.1410	65.1277
1000	0.75068	8.1674	65.3392
1500	0.75303	8.1930	65.5437

Table B2. Experimental data

	vacuum	vacuum DD	Press to 1500 psi	Drain 1500 psi	Draining 1000 psi	Draining 500 psi	Draining 250 psi	Draining 0 psi	Draining 1000 psi	Draining 500 psi	Draining 250 psi	Draining 0 psi	total collected
					Min						g		
Experiment 1	5	0	960	1440	1440	120			0.908	3.6793	2.0462	2.8768	9.5103
Experiment 2	5	0	960	960	1446	60	25	130	0.4079	2.9071	1.7003	2.7618	7.7771
Experiment 4	5	0	1023.6	384.6	1162.8	62.4	30	277.2	0.551	2.4717	2.7062	3.9091	9.638
Experiment 5	5	30	1014.6	300	990.6	184.8	114.6	120	0.4734	1.612	3.3049	1.6191	7.0094
Experiment 6	5	50	85	960	260	140	90	120	0.2959	1.7634	3.456	1.2479	6.7632
Experiment 7	5	30	960	190	150	65	55	1200	0.2234	1.1025	3.0133	2.9975	7.3367
Experiment 8	5	30	1200	405	1335	115	20	20	0.3014	2.7108	3.4212	1.7994	8.2328
Experiment 9	5	30	960	570	1080	120	135	20	0.2629	2.3783	1.8135	3.9755	8.4302
Experiment 10	5	30	960	570	1080	120	135	20	0.2702	2.3462	1.6832	3.9997	8.2993
Experiment 11	5	30	4320	210	1260	210	120	20	0.3106	2.6152	1.6799	3.7803	8.386
Experiment 12	5	30	4320	210	1260	210	120	20	0.242	2.3936	2.4456	2.2494	7.3306
Experiment 13	5	30	1020	1020	4320	210	121	20	0.4087	2.9385	0.5688	3.5465	7.4625
Experiment 14	5	30	1020	1020	4320	210	122	20	0.4388	3.0814	1.5004	2.6285	7.6491
Averages			1529	525	1304	136	88	179	0.3407	2.2945	2.3448	2.8987	7.8787

Table B3. Nitrogen density changes with pressure

Pressure	Nitrogen Density
psi	(g/ml)
0	0.001169
250	0.019923
500	0.040292
1000	0.079266
1500	0.11628

B3. References

Jamialahmadi, M.; Emadi, M.; Muller-Steinhagen, H. Diffusion coefficients of methane in liquid hydrocarbons at high pressure and temperature. J. Petroleum Sci. and Engin. 53. pp 47-60. 2006.

Upreti, s.R. and Mehrotra, A.K. Diffusivity of CO2, CH4, C2H6, and N2 in Athabasca Bitumen. Canadian J. of Chemical Engin. Vol 80. pp116-125. 2002.

APPENDIX C

Laboratory Investigations for Maximization of Production from Tight/Shale Oil Reservoirs: From Fundamental Studies to Technology Development and Evaluation

Micro-Scale and Visualization Studies

M. Voltolini, J. Ajo-Franklin and L. Yang
Lawrence Berkeley National Laboratory

C1. Objectives

- Comprehensive characterization of the Niobrara Shale, to provide quantitative information for models, to predict the possible evolution patterns of the rock under different conditions, and to provide a first insight to help choosing the best approaches for oil recovery.
- Use of 4D synchrotron x-ray microCT to better understand selected processes related to oil production techniques from tight shales at the μm resolution, at reservoir conditions.

C2. Characterization of the Matrix Properties in the Niobrara Shale

Within the laboratory investigation team associated with this project, we are working on a common set of natural geologic samples obtained from the Niobrara formation, an extensive shale oil target in the Denver Basin and beyond. The samples in question were quarried from an oil-bearing horizon of the Niobrara and LBNL was provided with a large block for project experimental purposes. While not fully representative of a single reservoir, quarried samples are attractive in that multiple large samples can be easily fabricated from a single block, presumably with similar properties, allowing parallel experimental efforts. However, due to the heterogeneity of the Niobrara formation, extensive characterization was required to provide a context for further experimental work.

Upon receiving initial samples from the Niobrara formation, we embarked on a comprehensive characterization study to inform the next set of in situ micro-imaging and core-flood experiments. The combination of electron microscopy, x-ray diffraction, and x-ray microCT, and provides a dataset including the mineralogy, chemical composition, and, texture/microstructure present in the sample. For the scanning electron microscopy (SEM) characterization two type of samples were prepared (**Figure C1**):

(1) Sample broken along the cleavage plane, sub-parallel to the bedding. This allows the morphological characterization of the phases and the planar features (SE imaging) of an undisturbed surface.
(2) Samples with a face cut and polished ~perpendicular to the bedding plane. This allows a better characterization of the microstructure/texture, better BSE images, and more reliable energy dispersive spectroscopy (EDS) analysis.

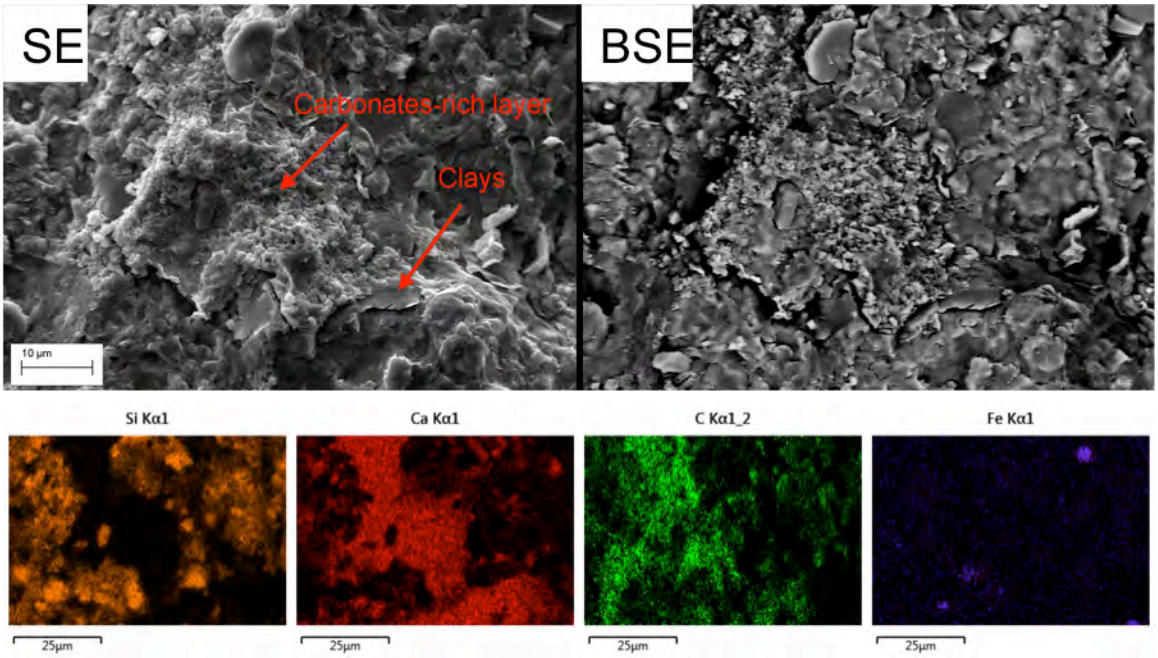

Figure C1. Top: Secondary Electron (SE) and Back Scattered Electron (BSE) images of the broken Niobrara sample. Bottom: elemental maps of key mineral components showing the distribution of the phases.

The x-ray powder diffraction (XRPD) experiment was carried out on a fragment crushed and pulverized from the same shale block, following a conventional procedure for lab XRPD measurements. The analysis of the XRPD profile was done with the Rietveld method, thus providing quantitative information about the bulk mineralogy, complementing the information obtained with SEM/EDS.

C2.1. Electron microscopy

The broken surface shows wavy structures at the tens of µm scale, with clay particles following the direction of these planes. Carbonates-rich structures also follow these planar features.

Organic-rich particles can also be found scattered on the sample surface. An example of an organic fragment can be seen in **Figure C2** (top left, yellow arrow) where the particle is found close to what seems to be a clay pseudomorph after feldspar.

The second Niobrara sample was cut and polished on a plane perpendicular to the bedding plane and more accurately captures the layering and textural features of the sample, as can be seen in **Figure C3**. This particular shale sample has a high carbonate fraction (mainly calcite) and the texture is strongly influenced by carbonate distribution. Carbonate zones are relatively diffuse in the shale, with occasional micrometric lenticular

structures enriched in calcite. Some carbonate layering at a larger scale is also present where calcite highlights again small lenticular structures surrounded by clays and quartz. The microporosity appears to be related to the calcite fraction; where calcite is present in larger amounts, the microporosity seems to be low (see BSE images). Some fine cracks healed with (often sparry) calcite are also present. In the figures presented the bedding direction is roughly vertical.

Organic-rich particles are also present as can be seen in **Figure C4** (BSE images and EDS maps, with a zoom of the particle). From the SEM analysis different accessory phases have also been identified including dolomite, pyrite (including typical framboids), and sphalerite/greenockite.

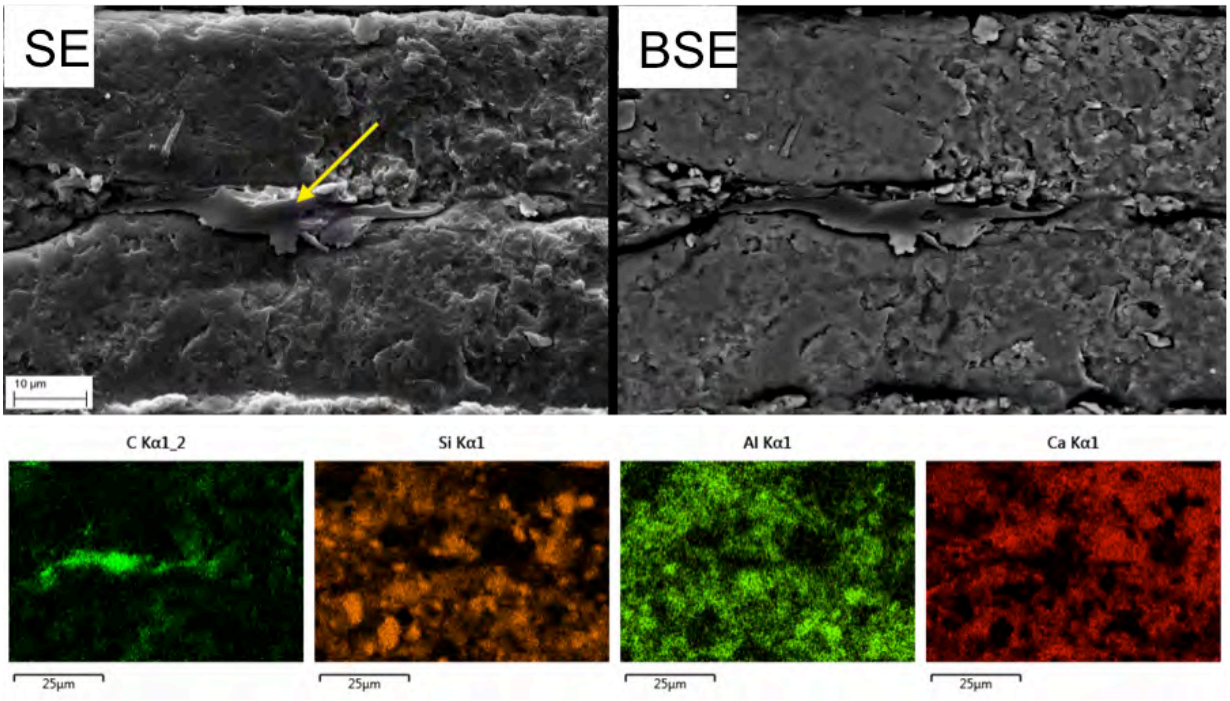

Figure C2. Example of an organic particle (yellow arrow). Top panels are structural images (SE/BSE) while bottom panels include EDS chemical imagery. The EDS maps confirm the carbonaceous composition of the particle.

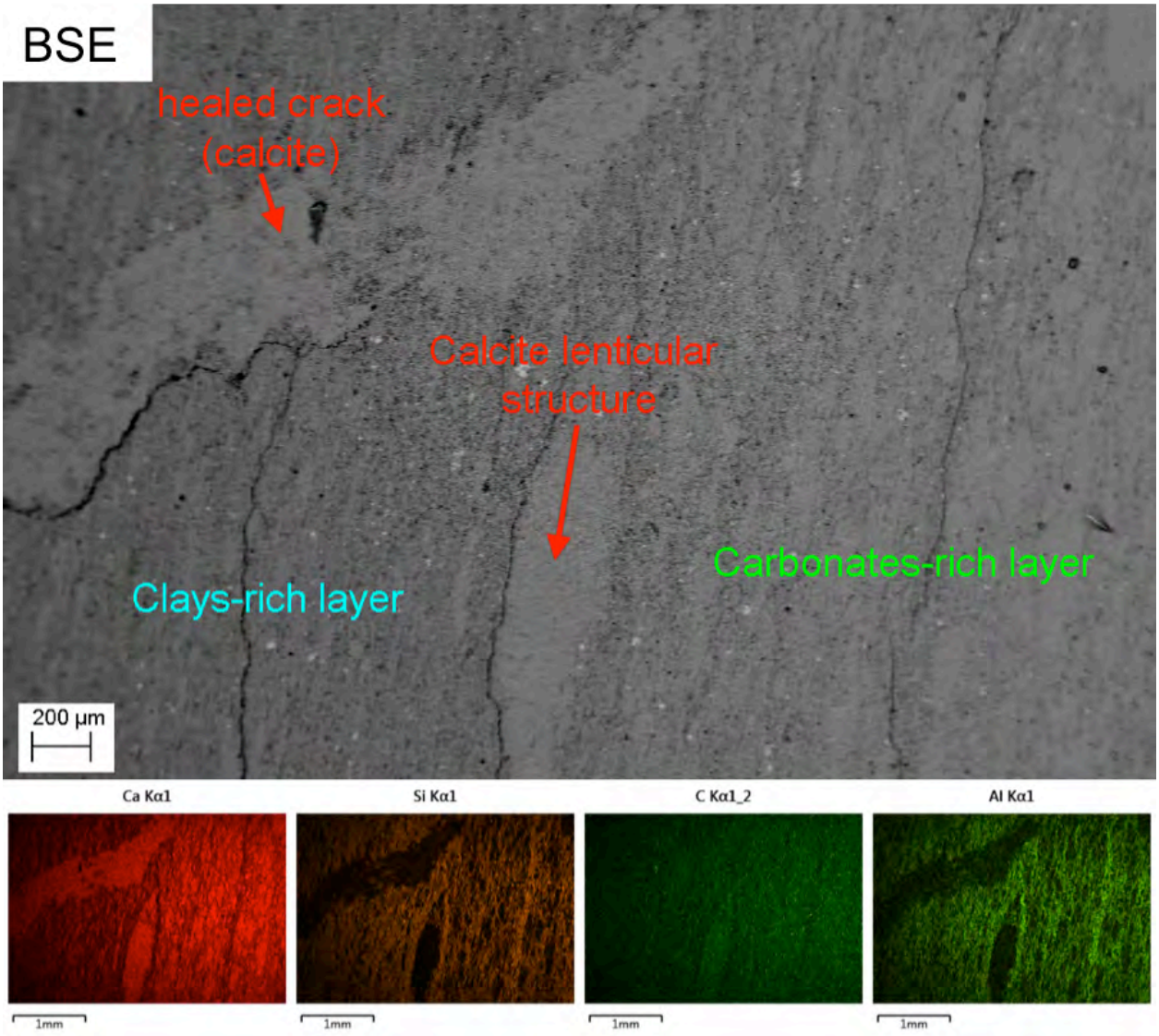

Figure C3. BSE (top) and EDS (bottom) maps of layered structure present in the sample. The EDS maps highlight the texture present on this sample, mostly due to the distribution of calcite (see Ca elemental map, bottom left).

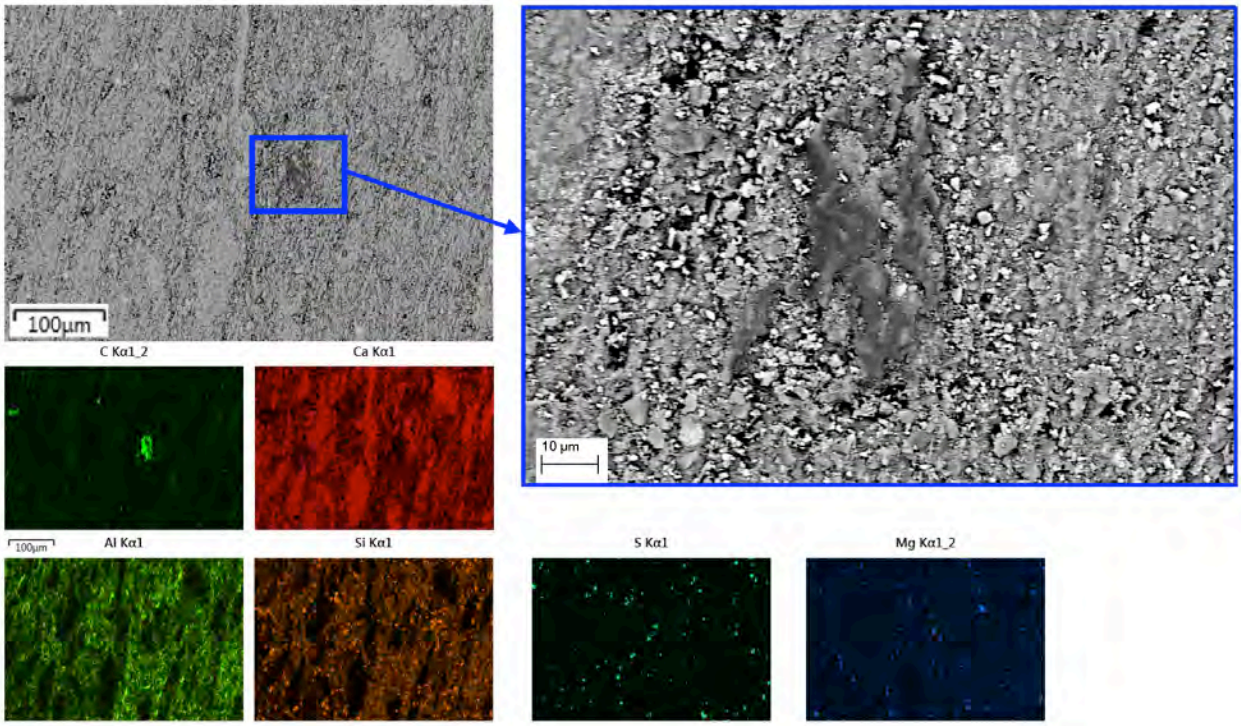

Figure C4. Example of an organic particle embedded in carbonate-rich layers (top BSE, bottom EDS).

C2.2. X-Ray Powder Diffraction analysis

To complete our initial characterization of the Niobrara shale sample, a fragment contiguous to the sample analyzed has been chosen and ground to a powder for XRPD analysis. The XRPD profile has been analyzed via Rietveld analysis to obtain quantitative information about the mineralogy of the sample.

Results are as follows [weight%(sigma referred to the last digit)]:
Quartz: 14.6(2)
Smectite (~14Å): 6.6(4)
Plagioclase: 3.5(3)
Calcite: 48.5(3)
Dolomite: 6.8(2)
Pyrite: 2.1(1)
Detrital mica - illite (modeled with a muscovite 2M1 structure): 17.5(4)

Lattice preferred orientation was considered for phyllosilicates and carbonates. Turbostratic disorder for the smectite has been included in this analysis. As it is possible to see, the carbonates (mostly calcite) comprise slightly more than one half of the sample by weight. The crystallinity of the sampled calcite is not very high (meaning not as high as in sparry calcite), as it is possible to appreciate from the peak shape function and to indirectly infer from the sample preparation (top loading sample holder for XRPD) that did not induce appreciable crystallographic preferred orientation. This confirms the observation from the SEM where the calcite looks more micritic in nature.

From this first characterization it is possible to see that this shale is very rich in carbonates (mostly calcite, with some dolomite), distributed in layers and in micrometric lenticular structures. The presence of the micritic calcite is also related to the microporosity of the sample. The clay amount is typical of many shales, with smectite (with significant structural/stacking disorder) and detrital mica, while other phyllosilicates such as chlorite and kaolinite seem to be absent. The organic-rich particles are scattered throughout the sample, and do not seem to follow the bedding by forming thin and flat structures like in many gas shales. Also, no significant porosity is visible at the magnification used for imaging.

C2.3. Static x-ray Micro-CT Analysis

To more thoroughly investigate the microstructure of the Niobrara shale, synchrotron x-ray (SXR) microCT was carried out on selected samples. This technique allowed us to obtain 3D data and study the sample in a perfectly undisturbed state (no need for vacuum or polished surface). The first observations obtained via SXR microCT confirm what seen using other imaging techniques: carbonates form lenticular structures surrounded by clay-rich layers a few μm thick. At a larger scale (~1mm) layering structures can be seen, highlighted by a different carbonates/clays ratio. Since the clay-rich layers are less attenuating, they are easily seen in SXR microCT datasets as darker layers (see **Figures C5** and **C6**).

The use of synchrotron radiation in this kind of analysis is advantageous since it is possible to take advantage of the monochromaticity and spatial coherence of the beam, and to choose proper compromises of resolution vs. field of view, to obtain very high-quality datasets. The facility used for these measurements is beamline 8.3.2. at the Advanced Light Source, at the LBNL.

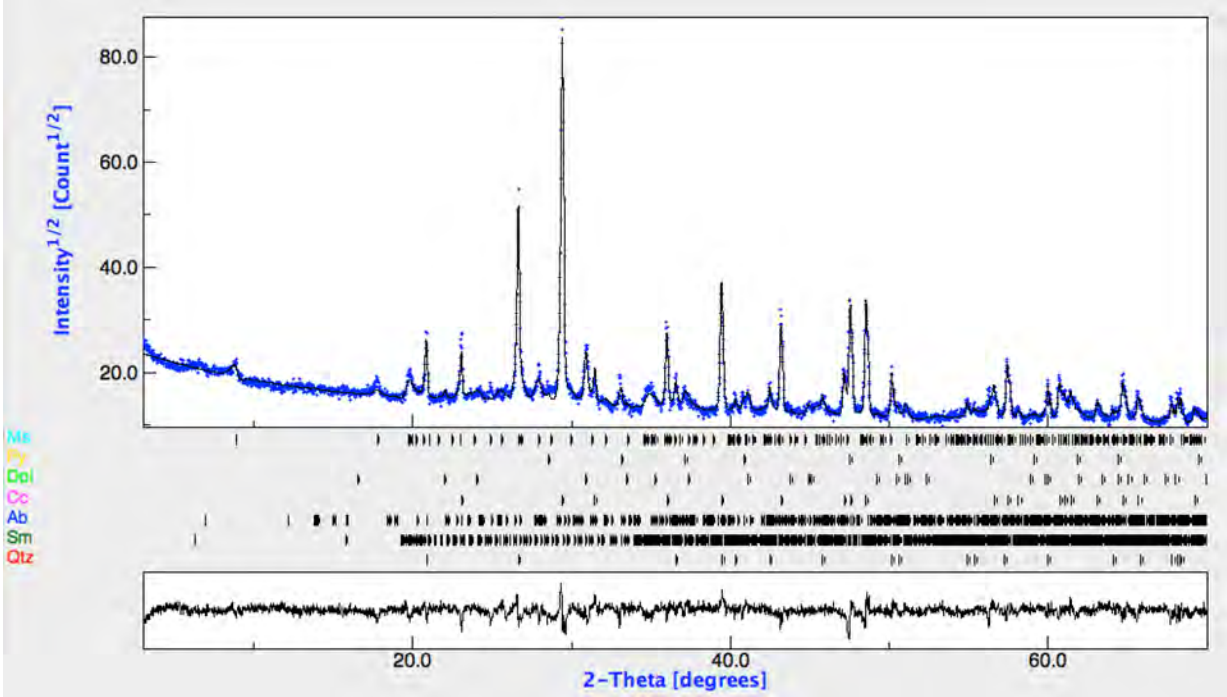

Figure C5. Measured and fit XRD profiles of Niobrara sample. Measurements are blue dots (top panel), and the Rietveld refined fitting curve is the black curve. As can be seen, measurements and the fitting curve are in good agreement.

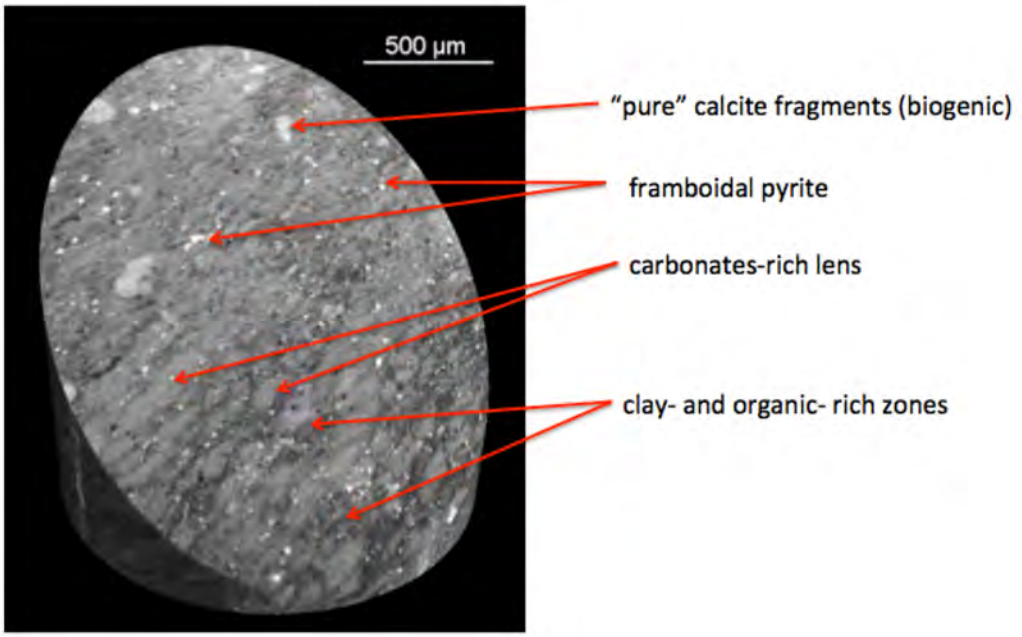

Figure C6. Virtual cut of a Niobrara sample measured with SXR microCT. The different mineral components and textural features as seen with SEM-EDS are visible also with this technique, giving a 3D context to the microstructure of the sample.

A preliminary investigation was also carried out to evaluate the potential of microCT for shale fracture imaging. A simple unconfined uniaxial breakage of samples was performed to see if the crack network generated could be related to textural features. In particular we wanted to see if the breakage of the sample would occur preferably in the clay-rich layers (**Figure C7**), a characteristic often encountered in shales (e.g., Mancos Shale). This preferential breakage can have an impact in the micro-fracturing behavior and also in the recovery of hydrocarbons, especially in case it would occur preferentially in hydrocarbon-rich layers. The geometry of the fracture surfaces is also important from a context of potential reactive surface area for a number of different processes. In this Niobrara sample we have not found any clear evidence that the breakage of the sample is *strictly* related to the clay-rich layers (**Figure C7** to C**9**), even though evidence of some preferential splitting behavior has been observed.

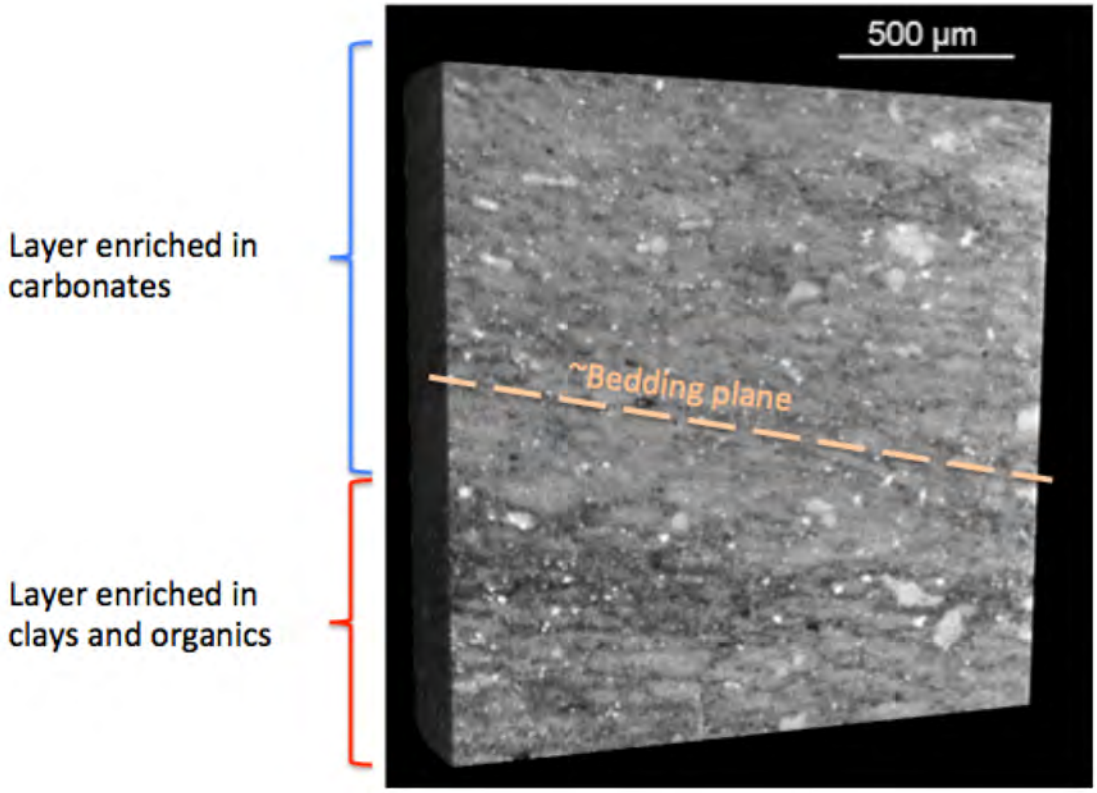

Figure C7. Virtual thin section of the sample, where a better image of the bedding features is shown. It is possible to appreciate the compositional differences highlighted by the different attenuation of x-rays at different scales.

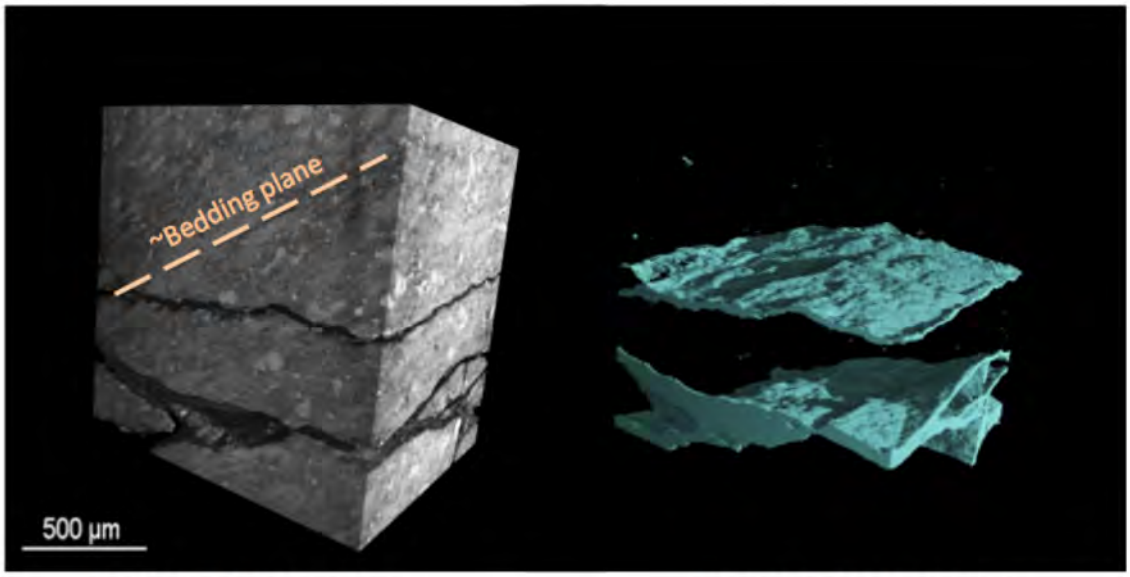

Figure C8. In this first experiment the fractures appeared irregular and seemed to be controlled primarily by applied stress state. They do not seem to be strictly related to the sample microstructure.

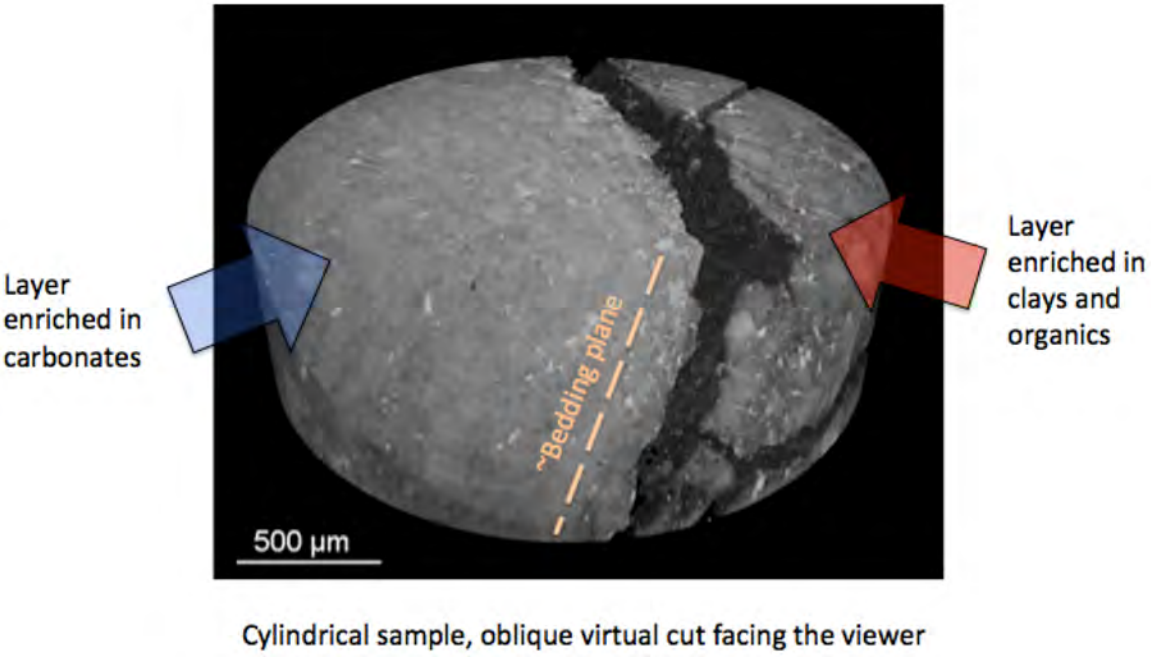

Figure C9. In this experiment the fractures look irregular as well, the main crack is has been generated at the interface of a clay-rich layer with a carbonates-rich layer, following the bedding plane. The clay-rich layer also shows a number of secondary fractures, while the carbonates-rich one is perfectly intact.

The material characterization via diffraction and electron imaging techniques, plus the starting, static, scans of the Niobrara shale samples, also provided an excellent starting point to plan the much more challenging dynamic SXR microCT experiments, aimed at understanding the behavior of oil shale at conditions compatible with hydrocarbon recovery processes in the reservoir.

It is worth to remark that the combined effort of beam-line 8.3.2 at the ALS and the Earth Sciences Division of LBNL for real-time imaging of geochemical processes at reservoir conditions is a continuing effort. At the same time, the local x-ray imaging facility is a worldwide pioneering capability for dynamic imaging (4D XR microCT) and has amassed probably the most extensive experience on geological materials, as evidenced from the publication and presentation record.

C.3. Laboratory Investigations: Fundamental Processes at the Pore to Fracture Scale

C3.1. Objectives

The *in situ* SXR microCT experiments carried out were aimed at answering two questions:

(1) How a fracture under a flow of carbonated water evolves. From a hydrocarbon recovery point of view, this is a critical assessment, since if CO_2 is used in the reservoir exploitation, and the reservoir rock is reactive at those conditions, significant modification of the microstructure and of the fracture geometry can occur. It is evident that if in the considered scenario the fractured behaves as self-sealing systems, the hydrocarbon recovery would be problematic. On the other hand, self-enhancing systems would increase the local permeability of the reservoir, thus potentially helping with the recovery of the product.

(2) The second question is related to EOR involves the utilization of liquid/supercritical CO_2 as a solvent to sweep hydrocarbons from fractured oil shales. The efficiency and the repercussion on the fracture aperture and crack surface microstructure of this process at the pore scale are still poorly understood and our experiment tried to shed some light on this unknown.

C3.2. Experiment 1: Monitoring the development of the fracture during flow of carbonated water

In this first experiment we have prepared a 3/8" x 1" Niobrara shale core, cut in half vertically to simulate a fracture along the sample. Bedding plane was chosen to be sub-horizontal to highlight eventual features due to different layers composition. The experiment was carried out using the in-house developed triaxial cell able to perform in-situ measurement at the SXR-microCT beamline. The experimental conditions chosen for this experiment were:

- Pore pressure = ~1400 psi
- Confining pressure = 1700 psi

- Fluid: equilibrated CO2-saturated water at 500 psi, ~25°C
- Flow rate: 5 µl/min during the first part of the experiment, 10 µl/min during the second part (to increase the extent of the reaction).

Experimental Results
The Niobrara shale showed some unexpected behavior. While the dissolution of the carbonates was relatively fast, as expected, the development of the surface of the fracture was different from any other rock investigated previously under similar conditions. Specifically, we observed the development of an unexpectedly wide weathered zone along the directions of preferential flow in the fracture, which was caused by the preferential dissolution of the carbonate-rich lenses (**Figures C10** and **C11**). The resulting less soluble material on the fracture surface, mostly clays and quartz/feldspar, is not easily mobilized by the flow of the reactant, but resides on the fracture surface for at least a few hundred microns of thickness.

The aperture maps (**Figure C12**) also show the development of the fracture geometry, with branching and the development of a "wormhole" structure with the evolution of the reaction.

From the slice above it is possible to see that the microstructure of the crack surface is not smooth, but apparently it follows the texture of the rock. This is to be expected since the lens-shaped structures are expected to dissolve faster than any other component. The SEM study in **Figure C13** also confirms this observation. From the SEM maps it possible to appreciate how the newly developed porosity is indeed due to the dissolution of the carbonate-rich lenses. A more interesting observation is that the residual clay-rich material is also enriched in organics (see C EDS map).

To summarize the information pertinent to EOR obtained with this experiment, it is possible to affirm that, in this context (mini-core, limited reaction time):
- There is an *increase in permeability* due to the *worm-holing* and preferential dissolution of carbonate-rich structures.
- Despite the development of a wide weathered zone along the preferential flow paths, the dissolution does not generate a significant change in the contact points in the fracture (so *the fracture is not closing* under the applied confining pressure)
- The weathered zone is *enriched in phases associated with the organic content* of the rock, potentially making them more exposed in case techniques involving oil solvents were employed.
- The weathered zone, made for a significant part from clay flocs, is also likely to have *weak mechanical properties* (important in case proppants are considered: es. sand grains would embed very easily in this layer, losing their ability to keep the fracture open).
- The *migration of fines is not significant*, thus leading to the development of the extensive weathered zone on the crack surface.

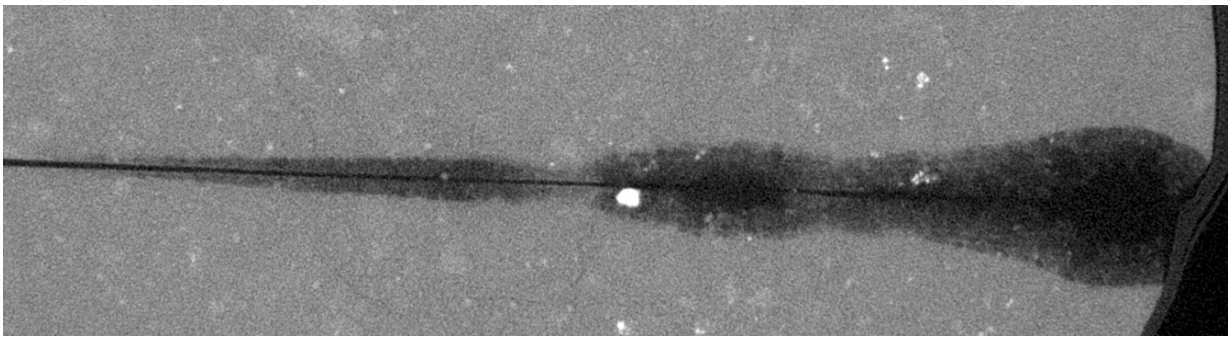

Figure C10. Horizontal cut of the sample after the reaction: the weathered layer developed on the crack surface and the preferential flow channels are evident. (image width: ~7mm)

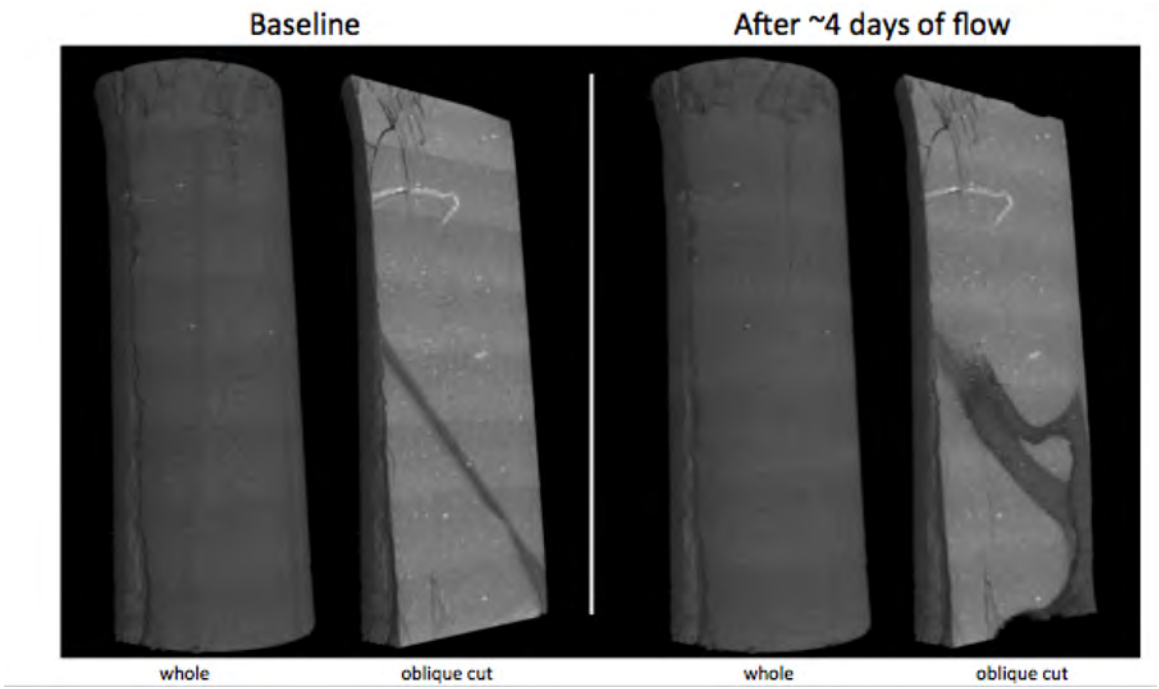

Figure C11. The entire sample, before and after the reaction.

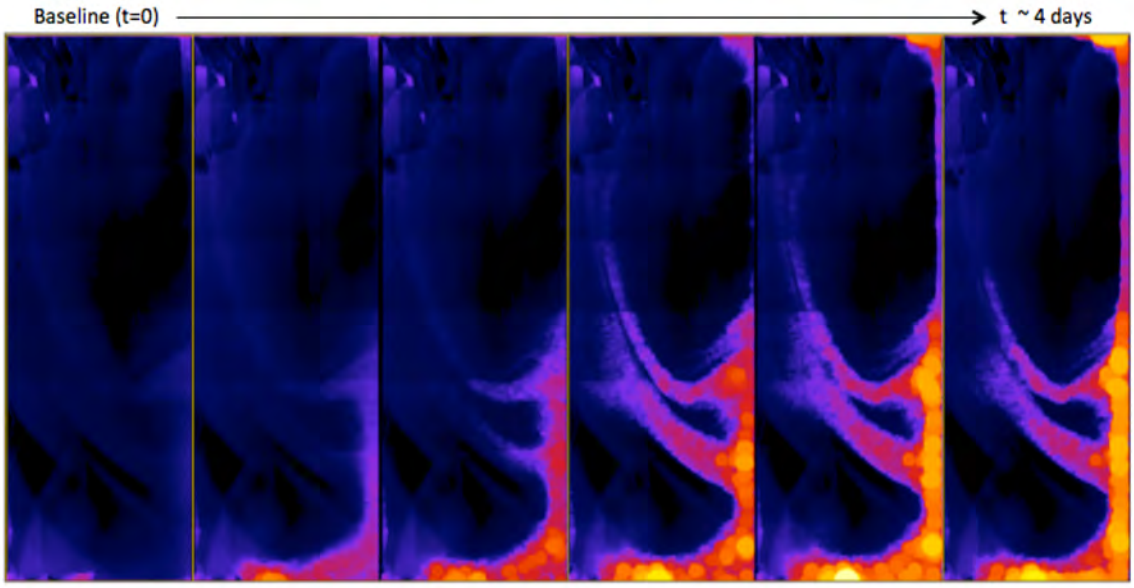

Figure C12. Local thickness aperture maps of the fracture at different stages of the reaction. Each step covers the whole sample with an area approximately of 3/8"x1". Inlet is at the bottom of the sample.

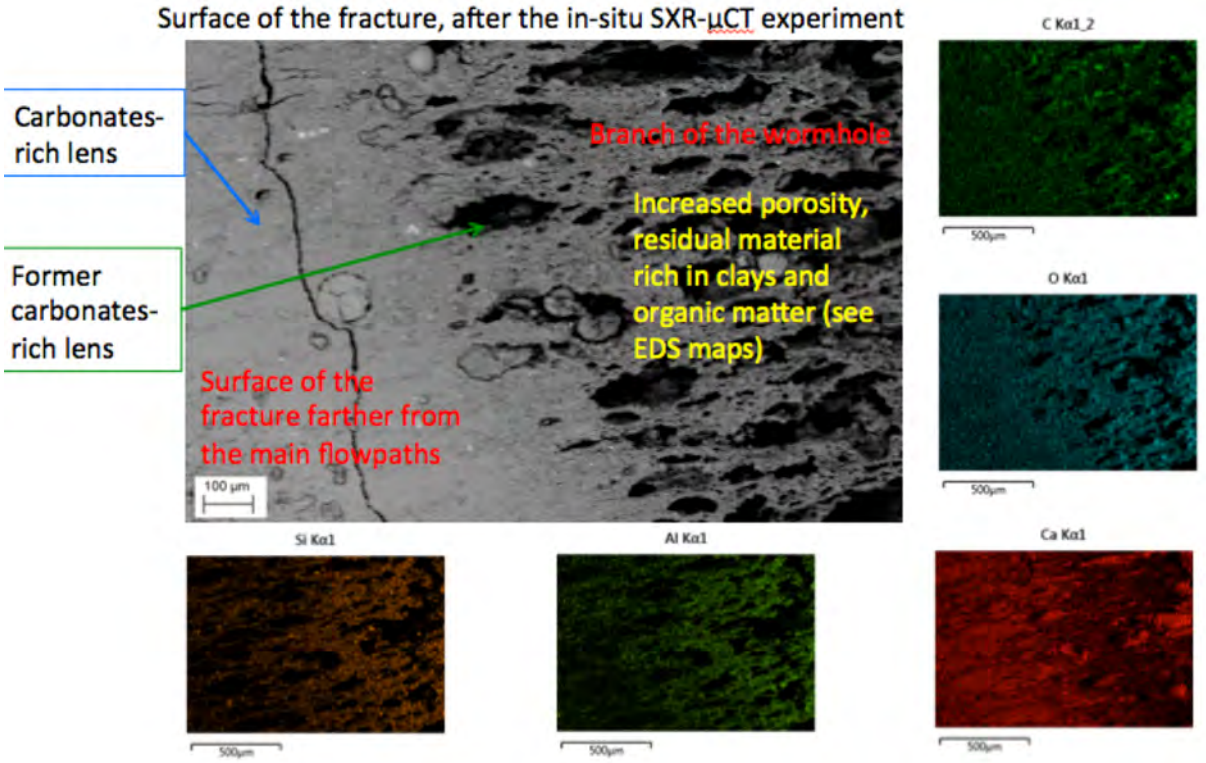

Figure C13. SEM analysis on one of the "branches" of the wormhole.

C3.3. Experiment 2: Effect of sweeping a propped fracture with liquid CO_2

In this second experiment we attempted to study the behavior of a water-saturated sample of Niobrara shale, with a fracture filled with proppant. Main goal was to monitor the solvent action of liquid CO_2 and eventual modifications to the fracture geometry, in particular proppant grain embedment in case of softening of the surface of the fracture.

The experiment was again set using the triaxial cell shown in **Figure C14**. The sample was a Niobrara core ~ 3/8" (diameter) x 1/2" (height) in size, cut in half and filled with a double layer of sand grains (20/30 mesh).

The sample was pressurized to a pore pressure of 1100 psi while confined at 1300 psi of hydrostatic stress. After this initial pressurization, a baseline microCT scan was acquired of the entire sample with an isotropic 6.87 μm voxel size.

Pure CO_2 was then compressed from gas to liquid phase (1100 psi, 24.6 °C) in an ISCO syringe pump and injected into the fractured sample at an initial rate of 100 μl/min for 3.25 hours followed by a first repeat scan. At this point flow was restarted at 25 μl/min for 11 hours followed by a second repeat scan. To the end of injection, approximately 36 mL of CO2 were injected through the fracture. After completion of the injection phase, another scan was taken increasing the confining pressure to 1700 psi, trying to induce fracture closure.

Experimental Results

The experiment showed extremely little change in the system. The first injection of liquid CO_2 generated a partial displacement of the water in the sample, but a significant amount of water was left in the fracture, thus limiting the contact of the solvent ($CO_{2(liq)}$) with the solvation target (the oil close to the fracture surface). Moreover, dissolution behavior, as described in the first experiment, is also limited, since a close to equilibrium state in the water with Ca^{++} and CO_3^{--}/HCO_3^{-} ionic species is quickly reached, resulting in just a limited amount of dissolution on the crack surface. This makes the whole system quite static, with exception of the two-phase flow: the solvation effect is limited by the pre-existing water, and at the same time the chemical reaction are significantly slowed down because of the fast saturation of the trapped water.

Figure C15 shows a rendering of the sample *after* the injection. In a reactive system it would be expected to see some modifications on the crack surface (to better appreciate this pert of the sample a series of virtual cuts are presented), more specifically a decrease in the x-ray attenuation values (~decrease in density) at the surface of the crack, but this effect is virtually undetectable. In the renderings different components have been segmented and labeled with different colors for clarity. The "shale" component has been left in gray scale to better highlight its texture and the (non-)presence of eventual weathered zones on the crack surface.

To better check for fine changes in the sample a further step in the analysis was taken. An equivalent vertical section of part of the sample was taken from the datasets before and after the reaction as can be seen in **Figure C16**. A registration procedure has been

employed to take into account the slight shifts of the sample due to mounting/unmounting, compression, etc. A difference of the registered images has been calculated to highlight where changes in grayscale (~density) are present. In the figure below the vertical slices pre- and post- reaction are presented using a different lookup table to better highlight the differences (A and B). Apart from the zone with the fluids, the two images look close to identical. In panel C, the pre-reaction vertical section (in grays) with superimposed a colormap where a decrease in attenuation values occurred is plotted. This color map highlights where the reactions in the sample happened. It is evident that the extent of the reactions is extremely low and concentrated in some parts of the crack surface, apparently far from the proppant grains, where the flow and diffusion are likely to be faster, and in these zones the extent of the reaction barely reaches 20 μm in thickness.

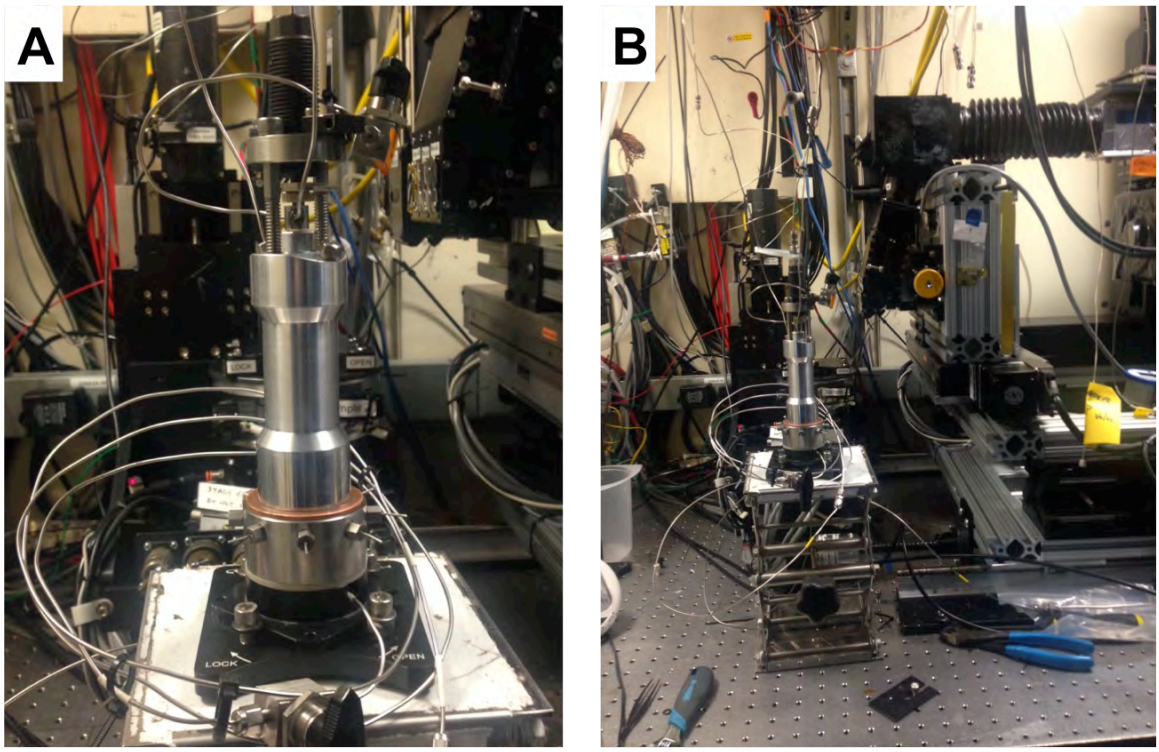

Figure C14. New HP triaxial cell for reservoir sample imaging at Beamline 8.3.2. Panel A shows a close-up of the refurbished micro triaxial vessel during the experiment while panel B includes the beamline hardware including the optics frame (on the right).

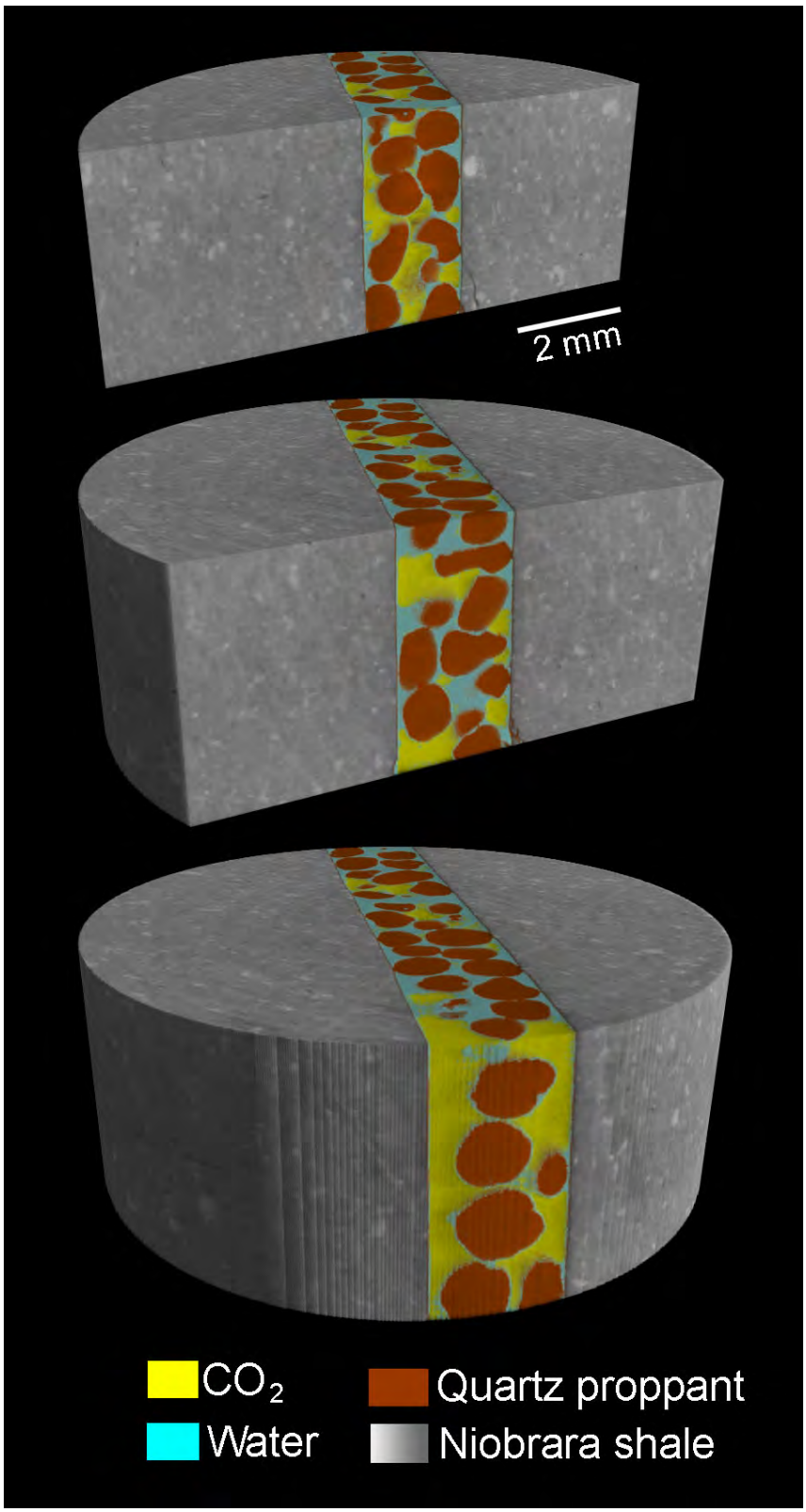

Figure C15. Cuts through the fractured Niobrara sample during liquid CO_2 injection. Niobrara shale matrix is shown in grey while the quartz sand proppant is shown in brown. The CO_2 and water phases are shown in yellow and blue respectively.

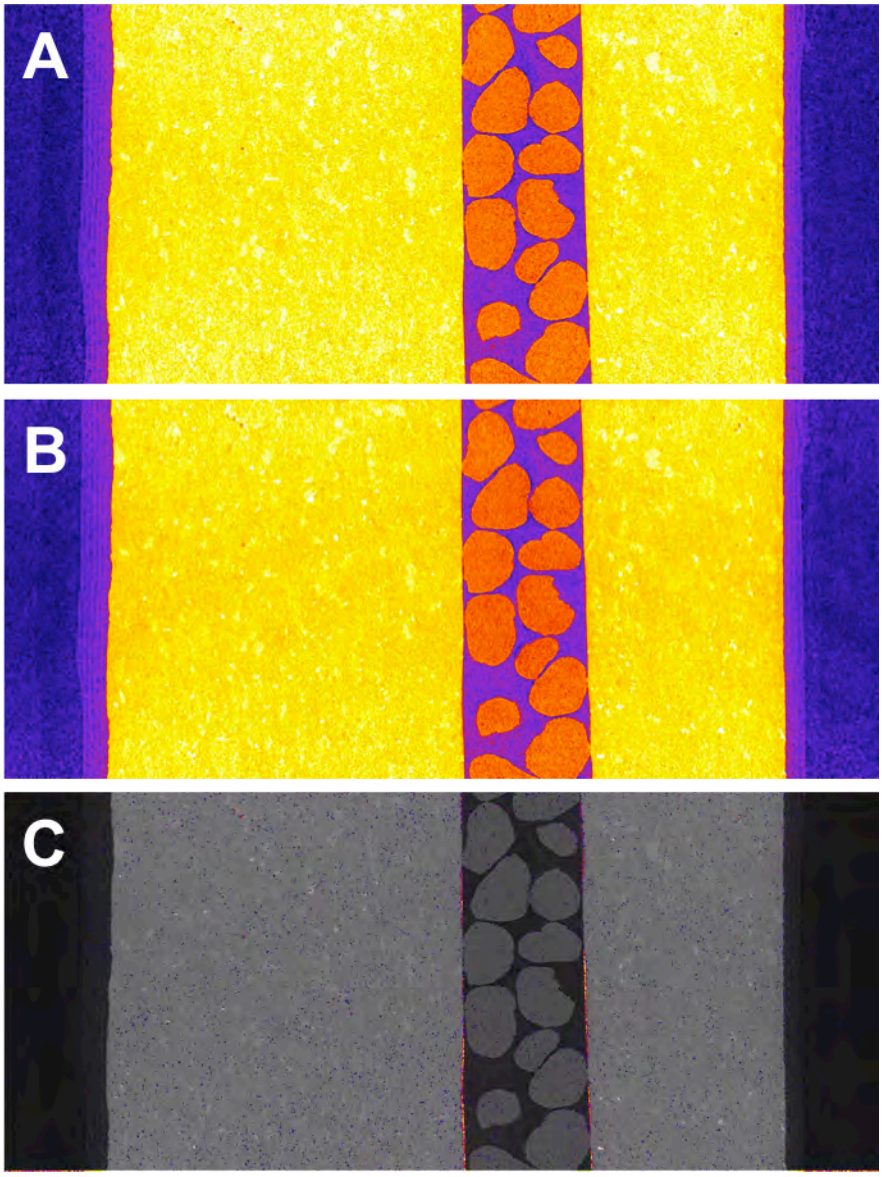

Figure C16. Cross-sections of tomographic volume showing near-fracture region before (A) and after (B) liquid CO_2 injection. Panel (C) shows the baseline image with color highlights in the narrow near-fracture regions which showed modification (only 2-3 voxels).

To summarize the results important from an oil recovery perspective obtained with this second experiment (we remark that the processes investigated with this experiment are limited to ~ one day):

- The water in the sample cannot be effectively displaced. Therefore *the effect of the solvent, the $CO_{2(liq)}$, is strongly limited* by the presence of the trapped water. This significantly limits the contact of the solvent with the oil close to the surface of the fracture.

- The trapped water and the two-phase flow also limits the transport of ionic species, thus creating a close to equilibrium situation in the water trapped at the contact with the crack surface, thus *inhibiting the dissolution of the carbonates on the crack surface*.
- Given the very limited modifications of the crack surface and the mechanical properties of the shale, in this experiment no variation of the fracture aperture is detectable when increasing confining pressure to 1700 psi (600 psi of differential pressure). The proppant is effectively keeping the fracture open.

APPENDIX D

Laboratory Investigations for Maximization of Production from Tight/Shale Oil Reservoirs: From Fundamental Studies to Technology Development and Evaluation

Molecular Fluid Dynamics Studies

G. Waychunas
Lawrence Berkeley National Laboratory

D1. Objectives

Development of the capability for accurately modeling dissolved and clustered hydrocarbons interactions with both clay basal and edge sites within model clay pores, while observing the effects of flow on these molecular units.

D2. Deliverables

The most important overall result would be the modes of interaction of hydrocarbon molecules with pore surfaces. These include collection of molecules at particular pore sites, i.e. aggregation of molecules, breakdown of hydrocarbons at reactive clay sites, reorientation of molecules near pore surfaces and in higher flow fields, and overall molecular migration. Other results would include that nature of coverage and sorption of hydrocarbon molecules on clay pore surfaces, with attention to the expected differing behavior at clay basal planes (more hydrophobic) versus clay particles edges (largely hydrophilic). Another aspect to be determined are the effects of pressure and temperature on hydrocarbon aggregation and movement, and the P,T conditions that are optimal to allow hydrocarbon migration through tight pores.

The work from this study may be extendable to more realistic dynamic simulations, such as larger clay particle aggregates (more complex pore structure), or to better realizations of flow effects, given more extensive computational ability. It should also be extendable to guide hydrocarbon-clay interfacial reaction calculations important in general biogeochemistry. Such reactions would include the breakup of hydrocarbon “clots”, solvation changes, vaporization into the accompanying gas phase, and others processes. These could be simulated with kinetic Monte Carlo approaches, perhaps buttressed with DFT (Density Functional Theory) energy calculations.

D3. Molecular Fluid Dynamics Simulation Activities

In order to model hydrocarbon-clay pore interactions one can take several approaches. Classical molecular dynamics (CMD) is a widely used approach for obtaining topological interactions between fluid molecules and a surface in a flow field. This technique has been used to examine molecular motion in a range of solids, including motion of hydrocarbons. It is thus a good starting point by which to assess favorable niches for hydrocarbon aggregation, and the effect of varied flow fields. However CMD contains no capability of modeling interfacial chemical

reactions, including changes in protonation, or any bond formation/breaking. It also depends crucially on the availability of interatomic potentials that span the full chemistry of the system. Gibbs Ensemble Monte Carlo (GEMC) approaches as developed by Panagiotopoulos can economically calculate fluid compositions in equilibrium with gas or any solid including phase transitions. Recent work (Kumar and Errington, 2013) allows transitional wetting interactions (such as oil-wet to water-wet) to be simulated. However this approach cannot assess reactivity or true chemical interactions. It does allow testing types of molecules and fluid compositions that may be at equilibrium at high P and T. Hence it can guide starting compositions for further MD-based simulations.

Reactive potential MD (RPMD) includes chemical reactions but has not yet been advanced beyond a limited set of atom types. Relevant self-consistent work has examined hydrocarbon interactions with silica surfaces (Pitman and van Duin, 2012; Joshi and van Duin, 2013). To extend this method to clays other cations (Na, K, Ca, Mg, Fe) need to be added to the reactive potential sets and thoroughly integrated with relevant testing. Higher level ab initio MD (AIMD) is the ultimate methodology, but inappropriate for large systems incorporating flow dynamics.

Another consideration is the manner of simulating flow in any MD-based simulations. Flow can be produced by adding an external gravitational forcing field to a system, or by resetting of molecular positions after a fixed number of time steps (such as by a process incorporated in the code OpenFOAM (Borg et al., 2010)). The latter essentially forces flow in the system without adding a false gravitational component but adds computational complexity and may be unrealistic on the molecular level. Not all ways of adding flow velocity to an MD system have been cross-evaluated for systematic prejudicing effects on simulation outcomes. Hence this aspect needs to be readdressed in analyzing results.

D4. Approaches and Results

To add in both chemical reactivity and flow effects to a MD aqueous hydrocarbon simulation in clay pores we will use existing knowledge of shale fluid compositions rather than try to survey them from a separate set of GEMC simulations. This is required due to the limited resources available under the proposal. We can then develop an improved set of potentials for RPMD starting with the potential set developed by the Van Duin group at PSU, and which effectively covers the basic chemistry and expected reactivity of idealized clay pores (ReaxFF). The Van Duin potentials include H, C, O, Si, Al and Cl (Van Duin et al., 2001).

As a first step we added Fe to their potential set, and tested this using simple structural models (silica surfaces, oxide surfaces in equilibrium with water) to determine if Fe coordinations in solution and Fe-O distances were reasonable, and that use of the new potential set yielded appropriate pair distribution functions for bulk water. Slight changes in the Fe potentials were made to get best agreement with all observations. This then yielded a “hydrid” potential set with most reactivity intact, but extended to include Fe. Further tests suggested that the set works well, and that the original reactive potential set could be extended in this way. The downside to this approach is that ideally all potentials should be recalibrated versus one another, a time-consuming task beyond the scope of the present project. Simulations of water pair-correlation

parameters compared to those measured by Soper et al. (1997) by neutron diffraction are shown in **Figure D1**. **Figure D2** is a movie of a water simulation over a slab of oxide.

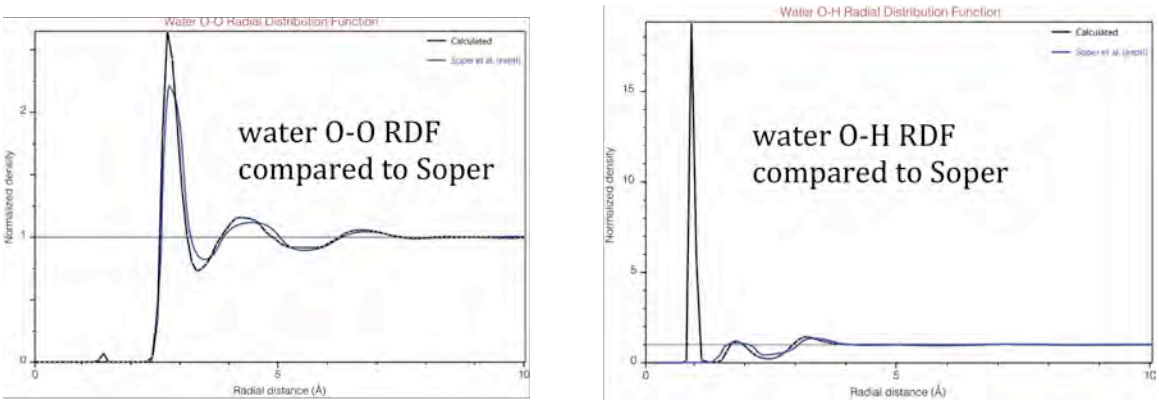

Figure D1. O-O and O-H pair correlations derived from water using hybrid reactive potentials compared to the data from Soper. Both interatomic diatances and density yield good agreement.

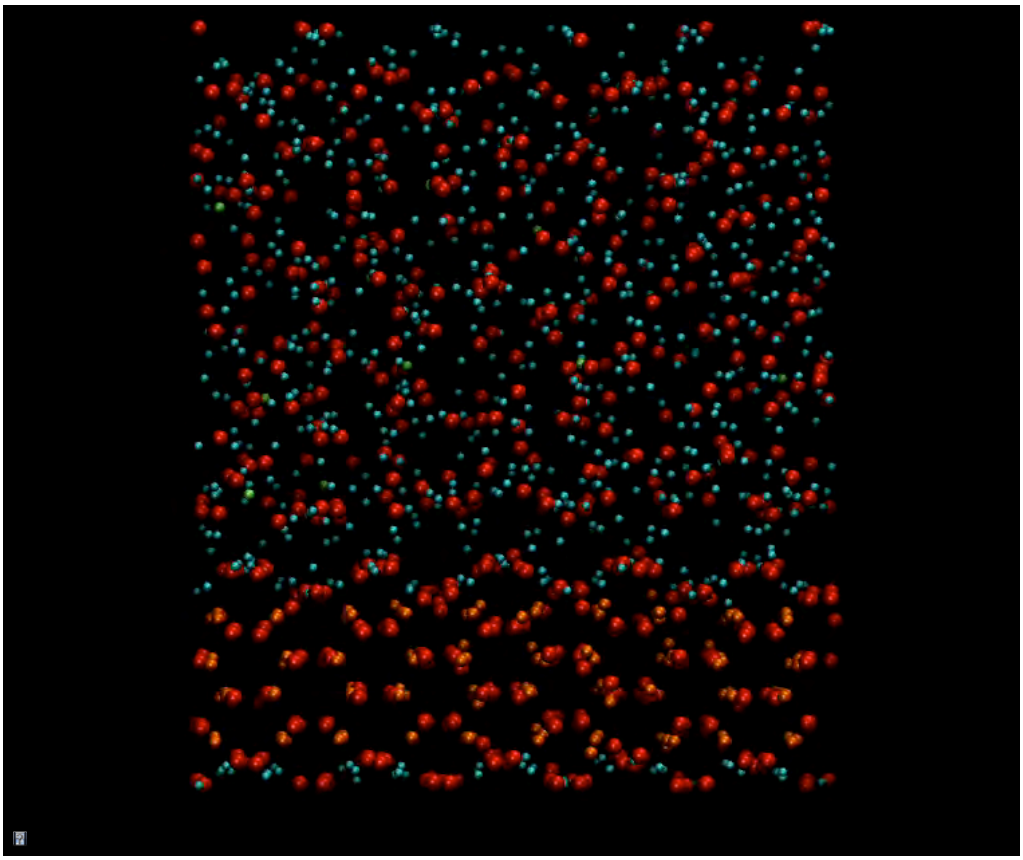

Figure D2. Simulation movie of water at ambient conditions using hybrid reactive potentials and the LAMMPS code. The surface is a model oxide slab with three types of oxygen sites. The aqueous solution also contains dissolved silica.

Next a "hybrid" potential for K was obtained to extend the new potential set to practical clay compositions. At this time this larger set is still being tested, with the use of a new structural model closely incorporating what we understand about clay surfaces and edges. Work now in progress will allow us to set up non-flow simulations for muscovite or illite clay compositions with a range of aqueous hydrocarbon fluids, and kaolinite and annite could also be simulated.

In order to proceed to the next step in the flow chart for this work (**Figure D3**) the results of these non-flow tests must be consistent with known experimental results for interface structure, solid-hydrocarbon and solid-water interactions. If there is disagreement the hybrid potentials may need to be adjusted to best-fit experimental results.

At this point we began exploratory runs of a series of simulations to examine the predicted reactivity of hydrocarbon molecules with clay surfaces. This uses the improved physical clay pore model shown in **Figure D4** with more than 10,000 atoms. The runs (in progress) examine aggregation at pore irregularities (such as the intersection of two grain surfaces), examine chemical breakdown at edge sites, examine possible hydrocarbon molecule injection into the clay interlayer, and test for catalyzed hydrocarbon reactions. The scope of the simulations will be adjusted as we proceed to optimize a direction toward the project objectives. For example, we may decide to modify the model topology to include geometries suggested by geophysical measurements, i.e. pore structure or size. Thorough evaluation of the static simulations is required before moving to a dynamic flow system.

The next, last step in the simulation program is to add the flow field by adding a gravitational force along the pore length. Flow rate will need to be high enough so that molecular interactions altered by flow can be characterized effectively. A valid question is whether high flow for short periods is an accurate extension of slower flow at longer times. Related to this is the issue of whether adding a gravitational force shifts molecular kinetic energies so as to make the system less ergodic. One way around this potential problem is the use of another (but more complex) approach to add fluid flow while not affecting ergodicity. This is, however, cutting-edge science requiring new code development and testing, both of which appear beyond the scope of the present project. This aspect might be considered in future project renewals.

D5. Leveraging Aspects

With generous support from DOE in terms of a computation-simulation summer student funded by the DOE CSGF program, we were able to take the first steps in working with and developing hybrid clay reactive potentials concurrent with the present project, saving considerable effort and time. Collaborative work using existing classical MD potentials (Clayff) has been initiated with the clay simulations group at LANL (Cygan and Greathouse, e.g. see Zeitler et al., 2014). This will be a continuing effort that encompasses parts of an ongoing DOE-BES project centered on mica edge reactivity (GW focus). This collaboration lends strength particularly to the testing part of the existing NETL work, as well as considerable expertise in MD simulations using the LAMMPS codes (Plimpton, 1995).

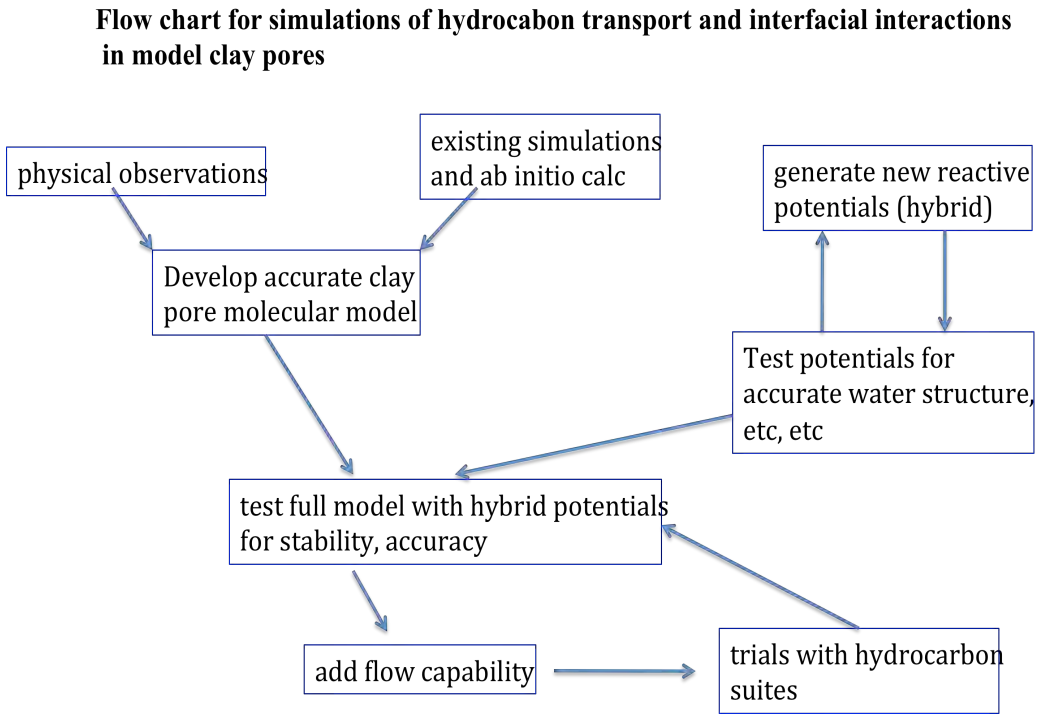

Figure D3. Flow chart for reactive potential clay pore simulation development.

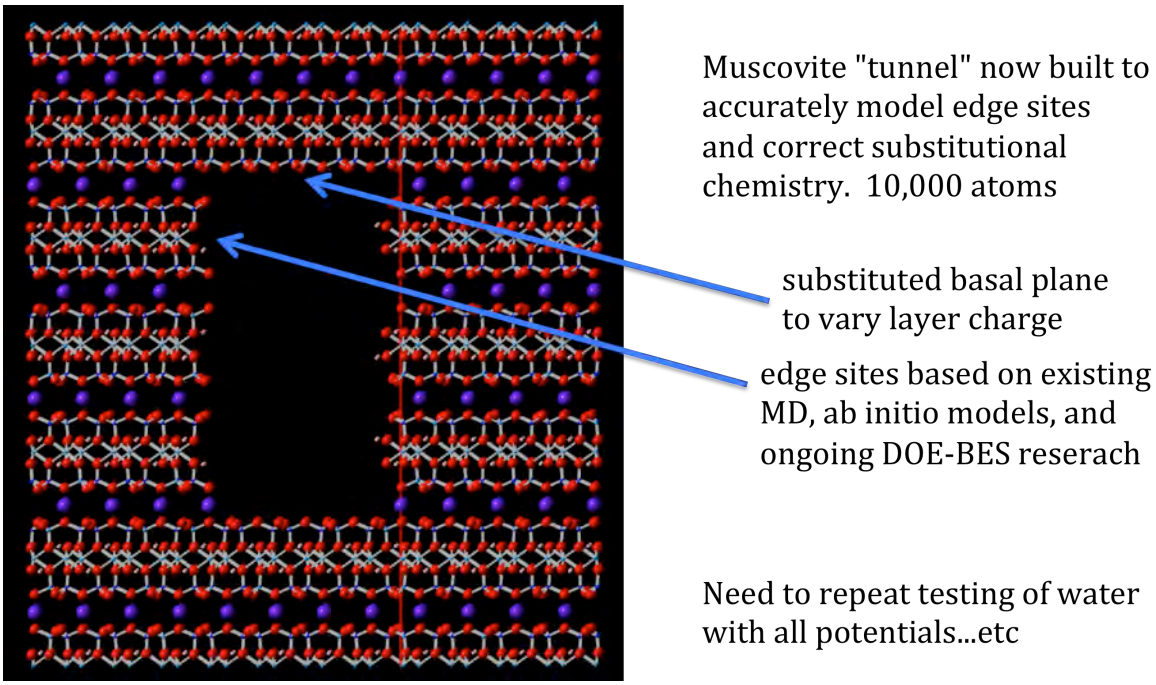

Figure D4. Clay pore model used in this study. Approx. 10,000 atoms are involved, including water in the pore itself. The internal surfaces are optimized for best agreement with existing edge models and both bond-valence and DFT calculations. (Red: oxygen; large purple: potassium; light blue: aluminum; dark blue: silicon; light brown: hydrogen)

The DOE-BES project at LBNL-ESD will be yielding new information on clay edge structure and reactivity that is not presently available (Liu et al., 2012; Bickmore et al., 2003). This information will be used in the present simulation study to allow improved pore simulation accuracy.

D6. DOE Facilities Usage

The HOPPER supercomputer at NERSC is being used for the needs of this project. Some clay/mica surface/edge work is being done at SSRL and APS involving DOE-BES leveraging research that will be useful for this project (e.g. composition and structure of clay particle edges).

D7. References

Bickmore et al. (2003) Ab Initio determination of edge surface structures for dioctahedral 2:1 phyllosilicates: Implications for acid-base reactivity. Clay Clay Minerals 51, 359-371.

Borg et al. (2010) Controllers for imposing continuum to molecular boundary conditions on arbitrary fluid flow geometries. Mol Sim 36, 745-757.

Joshi and van Duin (2013) Molecular Dynamics study on the influence of additives on the high-temperature structural and acidic properties of ZSM-5 zeolite. Energy Fuels 27, 4481-4488.

Kumar and Errington (2013) Understanding wetting of immiscible liquids near a solid surface using molecular simulation. J. Chem. Phys. 139, 064110.

Liu et al. (2012) Atomic-scale structures of interfaces between phyllosilicate edges and water. GHeochim. Cosmochim. Acta 81, 56-68.

Pitman and van Duin (2012) Dynamics of confined reactive water in smectite clay-zeolite composites. J Amer. Chem. Soc. 134, 3042-3053.

Plimpton (1995) Fast parallel algorithms for short-range molecular dynamics. J. Comp. Phys. 117, 1-19.

Soper et al. (1997) Site-site pair correlation functions of water from 25 to 400 C: Revised analysis of old and new diffraction data. J. Chem. Phys. 106, 247-254.

Van Duin et al. (2001) A reactive force field for hydrocarbons. J. Phys. Chem. A 105, 9396-9409.

Zeitler et al. (2014) Vibrational analysis of brucite surfaces and development of an improved force field for molecular simulation of interfaces. J Phys. Chem. C 118, 7946-7953.